Geophysical Journal International

Geophys. J. Int. (2026) **245,** 1–18
Advance Access publication 2026 January 23
Research Paper

https://doi.org/10.1093/gji/ggag030

High-resolution *P* receiver function imaging of seismic crustal structure in the southeastern Korean Peninsula: implications for deformation associated with Miocene backarc extension

Minkyung Kim [1], Hobin Lim [2], YoungHee Kim [1], Junkee Rhie [1], Tae-Seob Kang [3], Kwang-Hee Kim [4] and Jin-Han Ree [5]

[1] *School of Earth and Environmental Sciences, Seoul National University, Seoul* 08826, *Republic of Korea. E-mail: younghkim@snu.ac.kr*
[2] *Earthquake Research Center, Korea Institute of Geoscience and Mineral Resources, Dajeon* 34132, *Republic of Korea. E-mail: HBL@kigam.re.kr*
[3] *Division of Earth and Environmental System Sciences, Pukyong National University, Busan* 48513, *Republic of Korea*
[4] *Department of Geological Sciences, Pusan National University, Busan* 46241, *Republic of Korea*
[5] *Department of Earth and Environmental Sciences, Korea University, Seoul* 02841, *Republic of Korea*

Accepted 2026 January 20. Received 2026 January 16; in original form 2025 September 8

SUMMARY

Located at the easternmost passive margin of the Eurasian Plate, the southeastern Korean Peninsula shows geological signatures consistent with Miocene backarc opening associated with the Pacific Plate subduction. The region comprises two contrasting crustal blocks—the Early Cretaceous Gyeongsang Basin and Miocene Yeonil Basin (YB)—and hosts multiple fault systems that record both extensional and contractional deformation, providing an ideal setting to investigate crustal evolution along a passive margin. Motivated by this complex setting, we performed high-resolution *P*-receiver function imaging using a dense broad-band seismic network. Our results reveal two Moho offsets: a western offset from 33 to 28 km, and an eastern offset from 28 to 26 km, coinciding with major fault zones and likely reflecting localized crustal thinning and subsequent reactivation. Crustal anisotropy, inferred from changes in fast-axis orientations, varies spatially, with Miocene fossil anisotropy in the GB and both fossil and present-day stress-induced anisotropy in the YB. Variations in *P*-to-*S* velocity ratio (V_P/V_S) reflect compositional heterogeneity and fault-related fracturing. Large earthquakes ($M \geq 4$) occurred in low-V_P/V_S zones associated with relatively rigid and possibly locked crustal segments, while high-V_P/V_S regions coincide with zones of crustal weakening and microseismicity. Our findings suggest that extension-related deformation and inherited structural heterogeneity are preserved within the crust of this fossil backarc system, linking past tectonic processes to present-day structure and seismicity.

Key words: Body waves; Crustal imaging; Moho depth; Seismic anisotropy; Backarc basin processes; Crustal structure.

1 INTRODUCTION

Passive continental margins preserve long-lived structural and compositional imprints of lithospheric evolution, in contrast to active plate boundaries where ongoing deformation continually reshapes the lithosphere. High-resolution imaging of crustal velocity structures can therefore provide important insights into their tectonic histories. However, such studies have remained limited, largely due to the relatively sparse distribution of seismic stations compared with active plate boundary regions.

In this context, the southeastern Korean Peninsula provides a valuable example for understanding passive margin crustal structures. Located at the easternmost passive margin of the Eurasian Plate (Fig. 1a), the region preserves a deformed crust shaped by a complex tectonic history spanning from the Permian to the Miocene. The region is characterized by arc-related magmatism (K. Yi *et al.* 2012; H.O. Choi, S.H. Choi & S.S. Kim 2021), sedimentary basin formation (S. Chough *et al.* 2000; Y. Cheon *et al.* 2020; Y.I. Lee, J.I. Lee & Y.S. Choi 2023), dextral and sinistral strike-slip faulting under changing stress regimes (B.H. Hwang *et al.* 2007, 2008; Y. Cheon *et al.* 2019), backarc extension (Y.-I. Otofuji & T. Matsuda 1983, 1987; Y.-I. Otofuji, T. Matsuda & S. Nohda 1985; S. Lallemand & L. Jolivet 1986; L. Jolivet *et al.* 1992; L. Jolivet, K. Tamaki & M. Fournier 1994) and subsequent tectonic inversion into a compressional stress regime (J.H. Choi *et al.* 2015; M. Son *et al.* 2015; Y. Cheon *et al.*

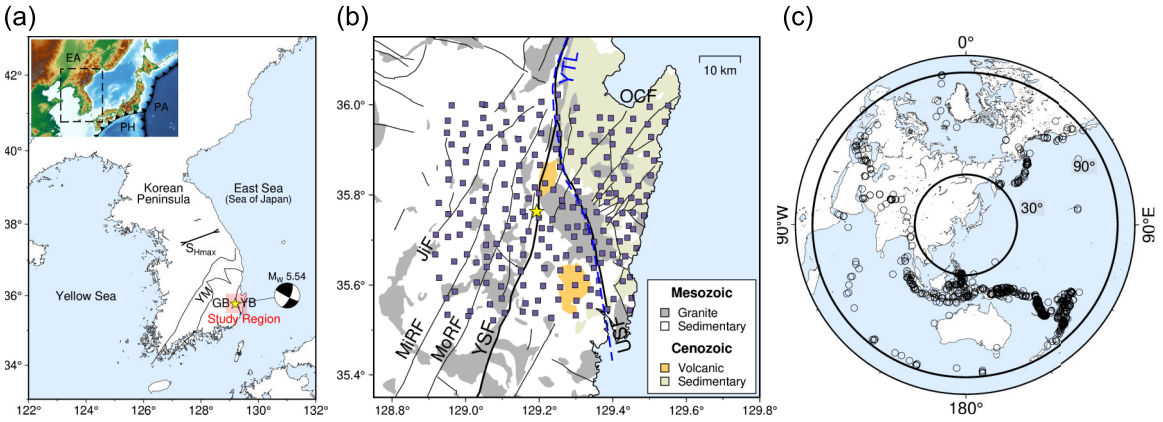

Figure 1. Maps of the study region and the distribution of seismic stations and earthquakes. (a) Tectonic framework of the Korean Peninsula with the inset indicating its position west of the Japan subduction zone, where the Pacific (PA) and Philippine (PH) plates subduct beneath the Eurasian plate (EA). Our study region, highlighted in the southeastern Korean Peninsula, includes the Gyeongsang Basin (GB) and the Yeonil Basin (YB). The focal mechanism of the M_W 5.5 earthquake on 2016 September 12 is shown (Y. Kim *et al.* 2016). The ENE–WSW orientation of maximum horizontal compressional stress (S_{Hmax}) is also indicated (Y. Park, J.-H. Ree & S.-H. Yoo 2006). (b) Map showing the distribution of seismic stations from the Gyeongju Hi-density Broad-band Seismic Network (GHBSN), marked with squares, overlaid on lithology and fault structures. Solid lines indicate fault zones; the dashed line indicates the Yeonil Tectonic Line (YTL), a geological boundary between GB and YB. (c) Distribution of 420 teleseismic earthquakes (epicentral distance of 30°–90°) used for RF analysis. Abbreviations: YM—Yeongnam Massif; YSF—Yangsan Fault; USF—Ulsan Fault; JiF—Jain Fault; MiRF—Miryang Fault; MoRF—Moryang Fault; OCF—Ocheon Fault.

2023). Although the region has transitioned into a tectonically stable setting since the Miocene, major fault systems—most notably the Yangsan and Ulsan faults—remain capable of generating significant seismic events, such as the 2016 M_W 5.5 Gyeongju earthquake (Y. Kim *et al.* 2016; 2017; K.-H. Kim *et al.* 2018; J.U. Woo *et al.* 2019). As a passive continental margin that has experienced multiple tectonic episodes, this region retains long-lived deformation imprints, highlighting the need for high-resolution imaging to characterize its crustal structure. Such imaging not only resolves its structures but also offers insights applicable to other passive margins. In this study, we construct a detailed model of the crustal architecture using data acquired from the Gyeongju Hi-density Broad-band Seismic Network (GHBSN), a dense array of 200 broad-band stations with an average interstation spacing of approximately 4.5 km (Fig. 1b), which were sequentially deployed from November 2017 in the aftermath of the 2016 Gyeongju earthquake.

The geophysical properties of the eastern Korean Peninsula show distinct signatures of past tectonic processes, particularly those associated with Miocene extension. Crustal thinning along the eastern margin of the peninsula has been attributed to this event (S.J. Chang & C.E. Baag 2007), accompanied by mantle upwelling, as inferred from regional gravity anomalies (S. Choi *et al.* 2023). Ambient noise tomography further indicates that continental rifting during the backarc opening facilitated magmatic underplating beneath the Moho and associated crustal uplift (S. Park & T.K. Hong 2024). P_n attenuation tomography reveals low *P*-wave quality factor (Q_P) beneath the offshore region of the East Sea (Sea of Japan), indicating strong attenuation and significant seismic energy loss, as well as low P_n velocity anomalies in the uppermost mantle beneath the southeastern peninsula (G. Yang *et al.* 2022). These features are interpreted as evidence of high thermal anomalies associated with upwelling of hot mantle material. Such thermal anomalies are thought to be related to horizontal mantle flow driven by slab rollback, contributing to the backarc opening during the Miocene (G. Yang *et al.* 2022). Rayleigh-wave anisotropic tomography reveals NW–SE-oriented fast directions in the southern East Sea, interpreted as fossilized lattice-preferred orientation (LPO) formed during the opening of the East Sea (X. Liu & D. Zhao 2016). Additionally, *P*-wave traveltime tomography indicates low velocity anomalies in the upper mantle at depths of ∼45 km, interpreted as evidence for weak mantle rheology resulting from partial melt and/or elevated temperature in the study region (S. Lee *et al.* 2023).

These geophysical observations are interpreted in the context of Pacific Plate subduction dynamics. Following the cessation of the Izanagi Plate subduction, the Pacific Plate began to subduct beneath the Eurasian Plate around 60 Ma (M. Seton *et al.* 2012; S. Liu *et al.* 2017; K. Liu *et al.* 2020; K. Yamaoka & S.R. Wallis 2023). The progressive steepening of the Pacific Plate's subduction angle, beginning around 30 Ma, caused slab rollback, which in turn facilitated mantle thermal upwelling and triggered backarc extension (Y.-I. Otofuji & T. Matsuda 1983, 1987; Y.-I. Otofuji *et al.* 1985; S. Lallemand & L. Jolivet 1986; Y. Tatsumi *et al.* 1989; L. Jolivet *et al.* 1992, 1994). This process, occurring over a relatively brief interval between the late Oligocene and middle Miocene (23–17 Ma), ultimately resulted in continental rifting and the separation of the Japanese Islands from the Eurasian Plate. This tectonic episode is widely regarded as the most significant geodynamic event in the western Pacific during the Miocene (T. Yamamoto & N. Hoang 2009; A. Van Horne, H. Sato & T. Ishiyama 2017), establishing the present-day eastern margin of the Eurasian Plate. Given its timing and geological impact, this event provides the primary tectonic framework for interpreting the present-day crustal structure in the region.

Within this broader geodynamic setting, the crustal blocks of our study region preserve distinct tectonic histories shaped by both Cretaceous and Miocene processes. The Gyeongsang Basin (GB), a non-marine sedimentary basin, was formed during the Early Cretaceous (∼120 Ma) as a result of Izanagi slab rollback (S.K. Chough & Y.K. Sohn 2010; Y. Cheon *et al.* 2020; Y.I Lee *et al.* 2023). In contrast, the Yeonil Basin (YB), located east of the Yeonil Tectonic Line (YTL), was affected by Miocene (∼20 Ma)

backarc extension, which led to the deposition of sedimentary rocks and volcanism (Fig. 1b). Seismic velocity models reveal slower *P*- and *S*-wave velocities in the upper crust of the YB compared to the GB, which are attributed to the presence of relatively unconsolidated Miocene sediments in the YB (S. Kim *et al.* 2016; S. Lee *et al.* 2023). Geophysical evidence further supports a boundary along the YTL: palaeomagnetic data from Tertiary rocks indicate north-oriented remanent magnetization west of the YTL and northeast-oriented magnetization to the east (I.-S. Kim *et al.* 1998; Y.S. Lee, N. Ishikawa & W.K. Kim 1999; M. Son *et al.* 2015). Despite their geographic proximity, the GB and YB record contrasting tectonic histories influenced by the backarc opening, providing constraints on the mechanisms of backarc extension, block rotation and subsequent crustal deformation.

Our study region is characterized by two major fault systems: the Yangsan Fault System (YFS) and the Ulsan Fault (USF), which have played a significant role in the region's tectonic evolution (J.-H. Ree *et al.* 2003; J.H. Choi *et al.* 2015). The YFS is a NNW–SSE-trending strike-slip system, comprising several subfaults, including the Jain Fault (JiF), Miryang Fault (MiRF), Moryang Fault (MoRF) and the Yangsan Fault (YSF) (Fig. 1b). Among these, the YSF is the primary structure within the YFS, extending over ∼200 km, while the other faults (JiF, MiRF and MoRF) are located to its west (Fig. 1b). East of the YSF lies the USF, a NNE–SSW striking low-angle thrust fault whose definition and characteristics remain a matter of debate.

Geophysical observations suggest fault-related anomalies along these systems. A low-velocity zone in the lower crust beneath both YSF and USF has been interpreted as a shear zone and/or a fluid-rich region (S. Lee *et al.* 2023). Geochemical evidence further suggests the ascent of mantle-derived fluids, consistent with the interpretation of this low-velocity zone as a fluid-rich domain and implying that the YSF penetrates into the lower crust (H. Lee *et al.* 2019; H. Kim *et al.* 2024). This interpretation is further supported by elevated heat flux anomalies observed along the fault zone (H.C. Kim & Y. Lee 2007; Y. Lee *et al.* 2010). Seismicity patterns also reveal that, although the USF is mapped at the surface as a linear low-angle thrust fault, its hypocentres are widely dispersed rather than confined to a single plane (D. Heo *et al.* 2024; J. Han *et al.* 2024). This contrast indicates that subsurface structure is markedly more complex than the surface mapping suggests. Geological observations complement these findings. Surface geology shows ∼20–30 km of lateral offset along the YSF, interpreted as the result of long-term strike-slip motion between ∼50 and 30 Ma, prior to the Miocene backarc opening (B.H. Hwang *et al.* 2007, 2008; Y. Cheon *et al.* 2020). This long-term movement produced a weak zone along the fault, which is further supported by drill core evidence of damage zones and localized magmatic intrusions (C.M. Kim *et al.* 2022). In contrast, recent studies suggest that the USF evolved into a thrust fault through the reactivation of a crustal weak zone initially formed during the backarc opening, following its cessation and transition to the present-day ENE–WSW compressional stress regime (J.-H. Ree *et al.* 2003; N. Kim *et al.* 2023; Y. Cheon *et al.* 2023).

In this study, we examine (1) the interaction between backarc extension and pre-existing weak zones, (2) the role of crustal anisotropy as evidence for extension-related deformation and (3) spatial variations in the *P*-to-*S* velocity ratio (V_P/V_S) as indicators of compositional and mechanical heterogeneities inherited from backarc processes. These factors have possible implications for present-day seismicity in this passive continental margin.

2 DATA

Following the largest recorded earthquake in South Korea—a moment magnitude (M_W) 5.5 that struck Gyeongju on 2016 September 12—the GHBSN was established in September 2017 to evaluate potential seismic hazards through dense observations of microseismicity. The GHBSN is centred around the epicentral region of the 2016 Gyeongju earthquake, covering a 60 km by 60 km area (Fig. 1b), with an average interstation spacing of 4.5 km and a sampling rate of 200 Hz. The network installation began on 2017 November 1 near the epicentral region, and was progressively expanded outward to cover a broader area. The deployment proceeded in several phases associated with rapid increases in the number of operating stations. Phase I involved the initial pilot installation, during which seven stations were deployed between 2017 November 1 and 2019 January 31. Phase II began on 2019 February 1, when the network expanded to 42 stations by 2019 March 16. Phase III marked the primary expansion stage: the number of operating stations increased to 117 on 2019 March 17 and reached the full 200 stations by 2019 September 7 (D. Heo *et al.* 2024). Station-specific deployment periods and location information are provided in Table S1.

In this study, we retrieved 647 teleseismic earthquakes of $M_W \geq 5.8$, occurring between December 2017 and October 2023, with epicentral distances of 30°–90°, in order to minimize the effects of upper-mantle discontinuities on wave propagation (Fig. 1c).

3 METHOD

3.1. Receiver functions

Receiver functions (RFs) are highly sensitive to seismic velocity discontinuities within the Earth's subsurface. In the *P*-wave RF method, the radial and tangential components are deconvolved by the vertical component to isolate converted phases. The *P*-to-*S* converted phase (Ps, referred to as Pms when generated at the Moho discontinuity) and reverberation phases (PpPs and PpSs + PsPs) between the Earth's surface and subsurface discontinuities can be identified in the radial RFs (Fig. 2a). This approach allows estimation of the depth of the velocity discontinuity based on the arrival time differences between the direct *P* phase and its converted phases. The amplitudes of the converted and multiple phases further help constrain the physical properties of the subsurface layers (Fig. 2c; C.A. Langston 1979; C.J. Ammon 1991; S. Rondenay 2009).

RF analysis also provides a useful tool for identifying crustal seismic anisotropy. In an isotropic medium, radial RFs exhibit no significant backazimuthal variation, and tangential RFs show negligible energy (Fig. S2a). In contrast, the presence of seismic anisotropy leads to backazimuthal variations in radial RFs and substantial energy in tangential RFs (Fig. S2b; A.W. Frederiksen & M.G. Bostock 2000). Analysing these variations allows for constraining azimuthal anisotropy, which provides critical insights into crustal deformation and related tectonic processes (H. Liu & F. Niu 2012; V. Schulte-Pelkum & K.H. Mahan 2014; J. Li *et al.* 2019).

RFs are influenced not only by vertical structure but also by lateral variations in Moho geometry. In the presence of a Moho offset (Fig. 2b), diffracted Pms phases appear as split pulses in the radial RFs, observable within specific backazimuthal ranges

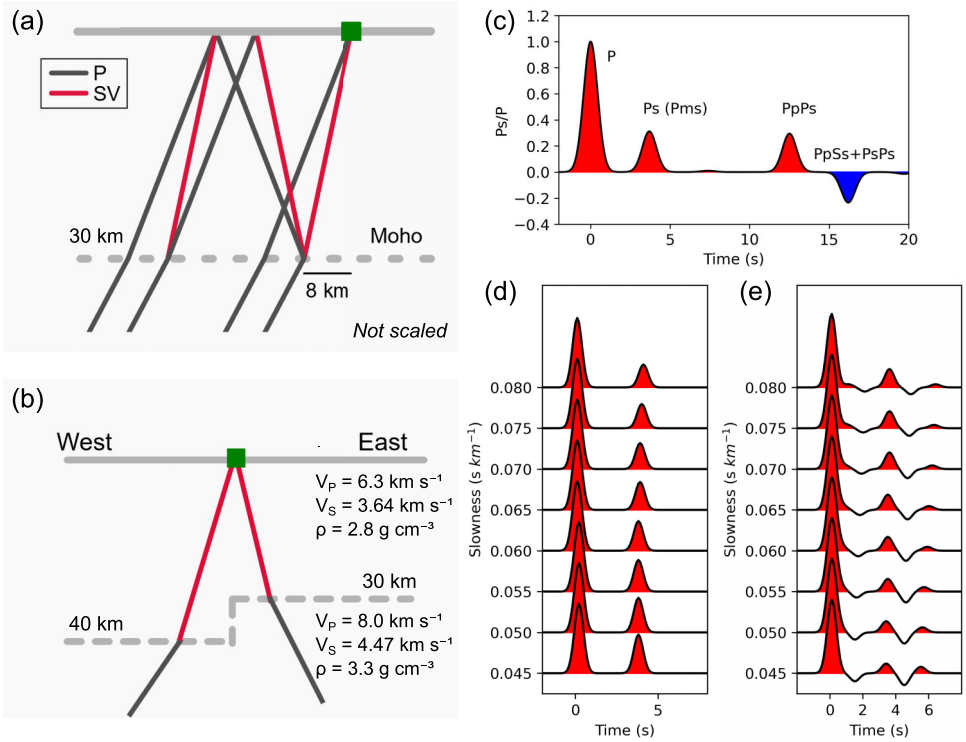

Figure 2. Synthetic RFs for flat and step-like Moho models. (a) Ray paths of an incident plane *P* wave and its *P*-to-*S* conversions beneath a flat Moho at 30 km depth. The piercing point radius of the Pms phase beneath the station (square) is approximately 8 km. (b) Ray paths for a step-like Moho, where the Moho depth transitions from 40 km to 30 km below the station. (c) Synthetic radial RF for the flat Moho model shown in (a), computed assuming a slowness of 0.06 s km^{-1}. The *P*, Pms, PpPs + PpSs phases are shown. (d) Synthetic RFs plotted against slowness for the step-like Moho model with western incidence, as illustrated in (b). The Pms near 4 s shows gradual variations in lagtime and amplitude with slowness. (e) Same as (d), but for eastern incidence. The Pms arrival is split into two positive pulses at 3.2–3.5 s and 5.8–6.1 s, and the time interval between the pulses becomes larger at higher slowness. All synthetic RFs are calculated using a Gaussian filter width of 2.5 and are scaled by the amplitude of the *P*-wave arrival. V_P: *P*-wave velocity; V_S: *S*-wave velocity; ρ: density.

of teleseismic events (Figs 2d and e), providing additional constraints on Moho structural complexities (Z. Yan & R.W. Clayton 2007; D. Shi *et al.* 2009). For the idealized step-Moho geometry shown in Fig. 2(b), where the Moho is deeper to the west and shallower to the east, RFs sampling from western backazimuths are expected to show a single Pms phase (Fig. 2d), whereas RFs from eastern backazimuths may exhibit split Pms phases due to diffraction at the Moho step (Fig. 2e). The systematic moveout of the split Pms pulses with slowness is consistent with diffraction-generated phases at a Moho step, which strongly depend on the incident angle. Such slowness-dependent shifts are reproduced in our synthetic tests only when a Moho offset exists (Fig. 2e), and have also been reported in previous studies (e.g. Z. Yan & R.W. Clayton 2007).

3.2. Pre-processing and receiver function calculation

Three-component seismograms were extracted from −30 to 90 s relative to the theoretical *P*-wave arrival time, calculated based on the IASP91 global model (B.L.N. Kennett & E.R. Engdahl 1991). The traces were then tapered, de-trended and bandpass filtered at 0.05–1 Hz (P. Goldstein & A. Snoke 2005; M. Beyreuther *et al.* 2010). We rotated the horizontal components of North and East to radial and tangential components using the misorientation angles reported by M.-S. Seo *et al.* (2022) with a particle motion-based method and re-evaluated in this study using an RF-based correlation-coefficient approach. Starting in April 2021, we observed that the tangential RF amplitude at 0 s exceeded that of the radial component at certain stations (e.g. Fig. S1a), which we interpreted as evidence of orientation changes. To correct these misorientations, we applied a grid-search method that maximized correlation coefficients of both radial and tangential waveforms (filtered between 0.05 and 1 Hz) between the target station and its nearby stations. Correlations were computed within a −20 to 20 s window relative to the theoretical *P*-wave arrival, with equal weighting for both components. The final orientation angle at each station was calculated as the circular mean of the grid-search results. Six stations deviated by more than 20° from the angles reported by M.-S. Seo *et al.* (2022); their codes and correction periods are listed in Table S2. Radial RFs were computed by deconvolving the radial component by the vertical component using the iterative time-domain method (J.P. Ligorría & C.J. Ammon 1999), and tangential RFs were similarly derived. A Gaussian filter with a width parameter of 2.5 was applied to all RFs, and the RFs were normalized by the amplitude of the direct *P* arrival. Only high-quality RFs, identified through manual inspection for clear Pms phase arrivals, were retained. After quality control, 19 616 pairs of radial and tangential RFs were obtained for subsequent analysis.

3.3. Stacking receiver functions

To estimate the Moho depth beneath each station, we employed both the H–κ stacking method (L. Zhu & H. Kanamori 2000) and

station-based stacking to capture regional trends and local variations in crustal structure. The H–κ method provides average crustal thickness (H) and V_P/V_S (κ) beneath each station. V_P/V_S serves as a proxy for crustal composition (e.g. silica content), offering insights into regional tectonics. On the other hand, the station-based stacking method allows for high-resolution imaging of Moho geometry, including localized offsets, and reveals lateral variations in crustal thickness that reflect complex deformation processes.

3.3.1. H–κ stacking method

This technique exploits the property that the arrival times of the direct *P*-to-*S* converted phase at the Moho (Pms) and its multiples (PpPs and PsPs + PpSs) vary systematically with slowness in the H–κ domain. This allows us to determine the optimal H–κ pair that best fits each phase arrival, thereby effectively mitigating the trade-off between H and κ.

In this analysis, we assumed a V_P of 6.3 km s^{-1} for the crust, which is the average crustal velocity in the Korean Peninsula (S.J. Chang & C.E. Baag 2006, 2007), such that the obtained V_P/V_S reflects variations in V_S. In addition, weighting factors of 0.7, 0.2 and 0.1 were assigned to Pms, PpPs and PsPs + PpSs, respectively, to optimize the stacking. To verify the reliability of the estimated H and V_P/V_S, we compared the theoretical arrival times of Pms and its multiples to those observed in the RFs, using the following traveltime equations (Figs S3c and d; A.W. Frederiksen & M.G. Bostock 2000):

$$\begin{aligned} t_1 &= t_{P_S} = H\left[\sqrt{V_S^{-2} - p^2} - \sqrt{V_p^{-2} - p^2}\right] \\ t_2 &= t_{P_PP_S} = H\left[\sqrt{V_S^{-2} - p^2} + \sqrt{V_p^{-2} - p^2}\right] \\ t_3 &= t_{P_SP_S+P_PS_S} = 2H\sqrt{V_S^{-2} - p^2}, \end{aligned} \tag{1}$$

where p is the slowness for each RF.

Uncertainties in H and V_P/V_S were obtained by dividing the standard deviation of stacked RFs in the H–κ domain by the square root of the number of events, representing a 68.3 per cent confidence interval (Figs S3a and b). The average horizontal distance between the piercing point of the Pms phase and its corresponding station is approximately 8 km (Fig. 2a), which we adopt as the effective radius of the H–κ stacking result. In regions where effective radii overlap, results were smoothed using weighting factors inversely proportional to both the square of the uncertainty and the distance from the station.

3.3.2. Station-based stacking

To enhance signal clarity and capture spatial variations in Moho depth, we performed station-based stacking after converting the time axis to depth using a regional 3-D velocity model (S. Kim *et al.* 2016). We converted time to depth using 1-D velocity profiles sampled from the 3-D model at each station. To investigate potential Moho offsets, we further divided the RFs by backazimuth into eastern (0°–180°) and western (180°–360°) groups and performed separate stacking for each group.

3.4. 2-D synthetic modelling

We performed 2-D waveform simulations using the OpenSWPC code (T. Maeda *et al.* 2017), a finite difference method-based solver for 2-D elastic wave propagation, to investigate the effects of a step-like Moho geometry on *P*-to-*S* converted phases. This synthetic modelling illustrates how lateral variations in Moho depth influence the appearance of split Pms phases as a function of backazimuth and incident angle. The synthetic RFs were computed using the velocity model shown in Fig. 2(b). The crustal velocity model assumes a V_P of 6.3 km s^{-1}, and a V_P/V_S of 1.73 (ideal Poisson solid) for deriving V_S. The uppermost mantle velocity is adopted from the IASP91 model (B.L.N. Kennett & E.R. Engdahl 1991). Density values for each layer are calculated using the empirical relation $\rho = 0.32V_P + 0.77$ (K.-A. Berteussen 1977). A source wavelength of 15 km was prescribed, which results in frequency content up to 1.058 Hz. For synthetic RFs, a Gaussian filter width of 2.5 was applied, and the RFs were normalized by the amplitude of the direct *P* arrival to enable consistent amplitude comparison of Moho-converted phases.

3.5. Estimating crustal anisotropy from joint analysis of the radial and tangential receiver functions

To quantify crustal anisotropy beneath each station, we applied the joint analysis of radial and tangential receiver function method of H. Liu & F. Niu (2012), which evaluates how seismic energy partitions between the two components as a function of backazimuth. In isotropic media, the tangential RF ideally contains no coherent energy (Fig. S2a); therefore, any systematic signal on this component indicates directional velocity dependence or structural dipping (Fig. S2b). By analysing these azimuthal variations, the method enables robust estimation of the fast symmetric axis (FSA) and delay time (δt), the two key parameters characterizing crustal anisotropy. This framework provides a physically consistent way to distinguish anisotropy from structural dipping and to assess the strength of anisotropic deformation.

Following the H. Liu & F. Niu (2012) framework, we performed a grid search over (FSA, δt) pairs and selected the combination for which the corrected radial and tangential RFs maximized radial coherence and minimized tangential energy (Fig. S2c). The procedure begins with a moveout correction to minimize slowness-related variation in Pms arrival times. The radial and tangential RFs are then projected onto fast and slow components based on an assumed (FSA, δt), and subsequently reprojected back to produce 'corrected' radial and tangential RFs.

When the optimal (FSA, δt) pair is applied, the Pms phases in the corrected radial RFs align at a constant arrival time when sorted by backazimuth, while the Pms amplitudes in the corrected tangential RFs are minimized. This principle forms the basis of the following three criteria used to estimate FSA and δt. First, the radial energy maximization with cosine moveout correction criterion (max(RCOS)) searches for the (FSA, δt) pair that maximizes the stacked Pms amplitude from the corrected radial RF, normalized by the amplitude in the uncorrected radial RF. Secondly, the radial correlation-coefficient maximization criterion (max(RCC)) maximizes the summed correlation coefficients among the corrected radial RFs, normalized by those from the uncorrected RFs. Thirdly, the tangential energy minimization criterion (min(T energy)) minimizes the stacked energy in the corrected tangential RFs, normalized by that in the uncorrected RFs.

While each criterion can independently determine (FSA, δt) pair, we adopted a joint objective function (JOF) combining the

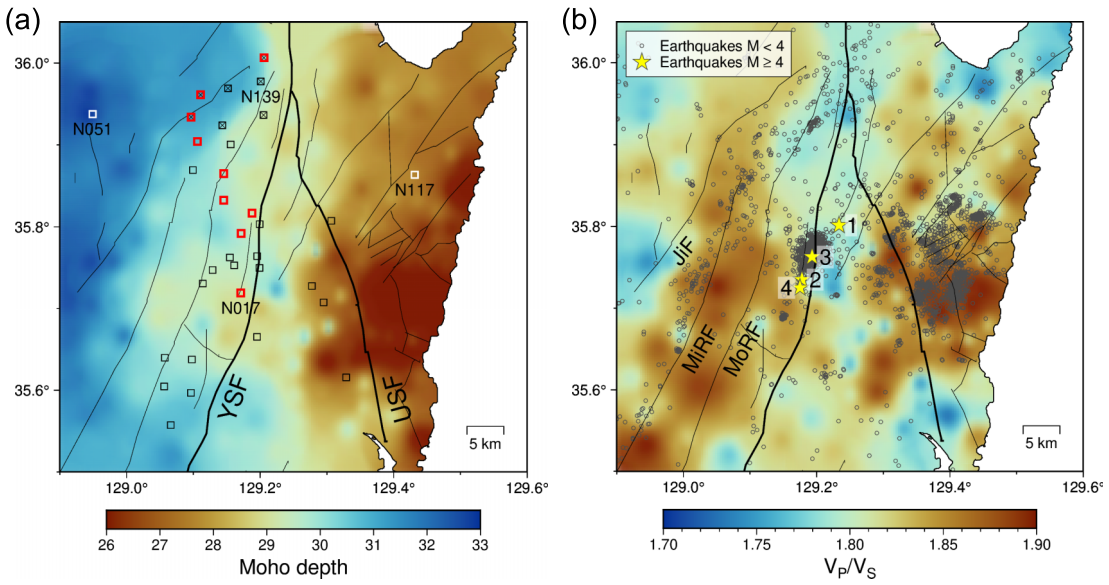

Figure 3. Constraints on the Moho depth (H) and *P*- to *S*-wave velocity ratio (κ; V_P/V_S) using the H–κ stacking method (L. Zhu & H. Kanamori 2000). (a) Interpolated H using all 200 stations shown in Fig. 1(b). Thirty-two stations showing split Pms phases are marked with open squares. Stations north of 35.9°N marked by open squares with an overlaid cross represent local Moho geometries that differ from the regional pattern. Red squares with bold outlines mark stations where the second Pms peak has a statistically larger amplitude than the first. (b) Interpolated V_P/V_S distribution. Yellow stars indicate four earthquakes with magnitudes greater than 4.0; the star labelled 1 marks the M_L 4.2 earthquake on 1997 June 26 (T.W. Chung & W.H. Kim 2000), while labels 2, 3 and 4 correspond to the foreshock (M_W 5.1), the main shock (M_W 5.5), and the largest aftershock (M_W 4.3) in September 2016, respectively (Y. Kim *et al.* 2016, 2017). Open circles represent smaller seismic events ($M < 4.0$) which occurred from November 2017 to December 2021 (D. Heo *et al.* 2024). Examples of H–κ stacking results for stations N051 and N117 are shown in Fig. S3. JiF: Jain Fault; MiRF: Miryang Fault; MoRF: Moryang Fault.

three criteria with different weighting factors. Due to high noise levels in the tangential RFs, we assigned weighting factors of 0.5, 0.4 and 0.1 to max(RCOS), max(RCC) and min(T energy), respectively. A grid search was performed over the parameter space, varying FSA from 0° to 360° in 1° increments and δt from 0.0 to 1.5 s in 0.01 s increments. All criteria were evaluated within a fixed time window of 2–6 s, which is sufficiently broad to accommodate $\pm\delta t/2$ shifts around the typical Pms arrival time (3–5 s) observed in previous RF studies in the Korean Peninsula (e.g. S.J. Chang & C.E. Baag 2007). Due to the inherent 180° symmetry in azimuthal anisotropy, the JOF provides two equivalent maxima at FSA and FSA + 180°, which are treated as one solution. The peak amplitude of the JOF reflects the strength of anisotropy; only measurements with JOF amplitudes exceeding 1.1 are considered reliable. Finally, we validated the anisotropy estimates by comparing observed RFs to synthetic RFs generated using the Raysum code (A.W. Frederiksen & M.G. Bostock 2000), with isotropic parameters from H–κ stacking and anisotropic parameters derived from the joint analysis.

4 RESULTS

4.1. General trend of the Moho depth from H–κ stacking

Our H–κ stacking results reveal clear regional variations in crustal properties. The uncertainties in H and κ are sufficiently small to permit meaningful interpretation. Across the study region, both H and V_P/V_S exhibit significant lateral variation, with Moho depths ranging from 24 to 34 km (Fig. 3a) and V_P/V_S from 1.70 to 1.90 (Fig. 3b). A first-order observation reveals a general eastward shallowing of the Moho. To quantify this trend, we performed a planar fitting analysis in Cartesian coordinates, which yielded a dip of 6.7° towards the west-northwest (Fig. 3a).

4.2. Spatial variation of *P*-to-*S* wave velocity ratio

The average V_P/V_S in our study region is estimated to be 1.82. Locally, low V_P/V_S values (< 1.73) are observed near the epicentral areas of the 1997 and 2016 Gyeongju earthquakes—labelled 1 through 4 in Fig. 3(b)—as well as near the intersection of the YSF and USF near 35.9°N, 129.2°E. In contrast, high V_P/V_S regions (> 1.85) are found near the MiRF and MoRF, and in the eastern region of the USF around 35.75°N, 129.4°E. These high V_P/V_S regions generally correspond to areas of high seismicity of magnitude lower than 4, with the exception of the 2016 Gyeongju aftershock zone and the YSF–USF intersection zone.

4.3. Observation of a two-step-like Moho geometry

RFs stacked using the station-based method reveal a dipping Moho discontinuity along profiles A–A′, B–B′, C–C′ and D–D′, which are aligned roughly parallel to the dip direction (Fig. 4a). Positive Pms phases appear at depths of 26–33 km and systematically shallow eastwards along these profiles (Figs 4b–e), suggesting the presence of sharp vertical offsets over short horizontal distances.

As described in Section 3.3.2, Moho offsets can produce azimuthal variations in the Pms arrival. To investigate this, RFs were divided by backazimuth into eastern (0°–180°) and western (180°–360°) groups and stacked separately (Fig. 5). Fig. 5(a) schematically illustrates symmetric Pms expected from a flat

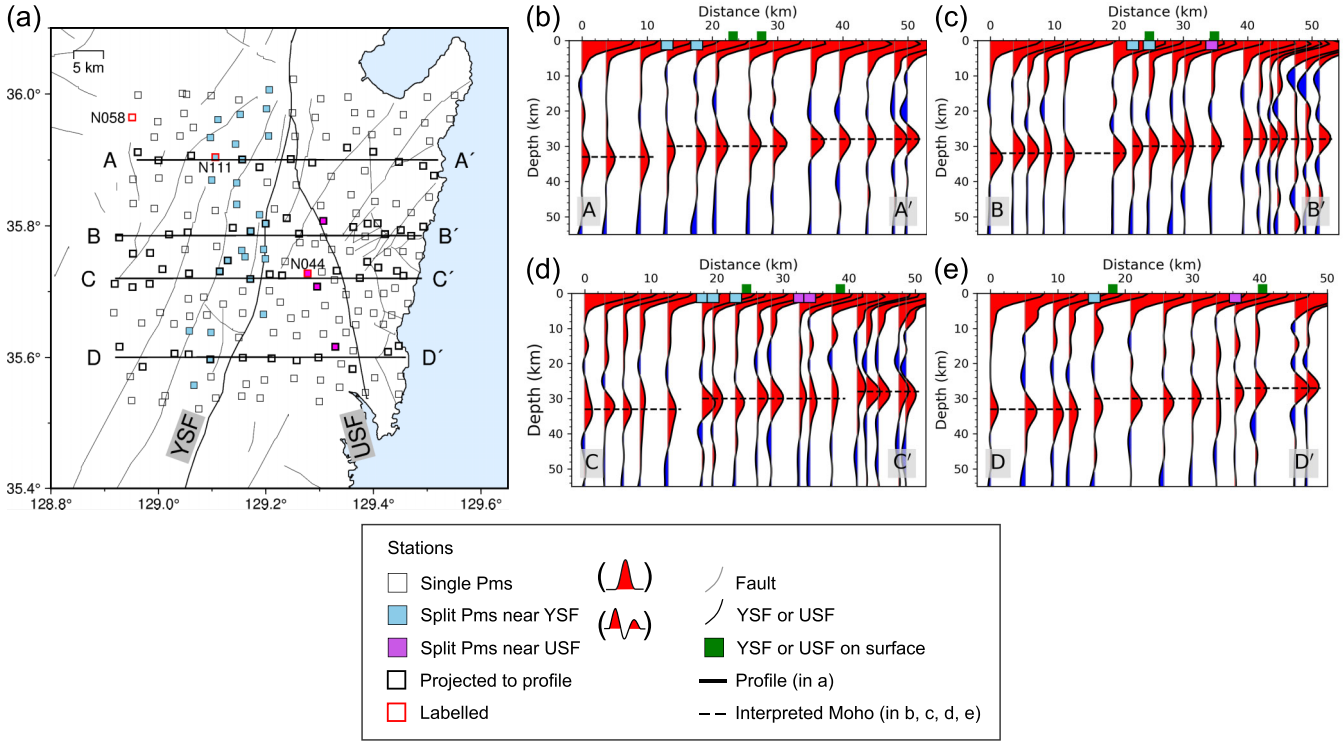

Figure 4. Station-stacked radial RFs. (a) Locations of stations and profiles A–A′, B–B′, C–C′ and D–D′. Stations are categorized based on Pms phase characteristics: stations with single Pms phases are shown as white squares, while those with split Pms are shown as coloured squares. Among the split-phase stations, those near the YSF are marked in light blue, and those near the USF in purple. (b–e) Station-stacked radial RFs along profiles (b) A–A′, (c) B–B′, (d) C–C′ and (e) D–D′. Dashed lines indicate interpreted Moho discontinuities.

Moho, whereas Fig. 5(b) shows split Pms for a step-like Moho geometry. In the latter case, an earlier high-amplitude pulse is followed by a later low-amplitude pulse (Fig. 5b, black dot) due to diffraction across a sharp vertical offset.

In A–A′ (Figs 5c and d), vertical offsets of ∼5 km (between 13 and 18 km) and ∼2 km (around 35 km) are visible in both western and eastern backazimuth stacks. Similarly, in C–C′ (Figs 5e and f), offsets of ∼5 km (between 18 and 23 km) and ∼2 km (between 32 and 35 km) are observed. Notably, the split Pms phases are more prominent in the eastern stacks (Figs 5d and f). Likewise, RF stacks for B–B′ and D–D′ profiles, divided by backazimuth, are shown in Fig. S4. The 32 stations exhibiting split Pms are shown in Fig. 4(a). These stations display split pulses in the eastern backazimuths, indicating that the shallower side of the Moho offset lies eastwards (Figs 2d and e). This spatial pattern is consistent with the overall eastward shallowing trend of the Moho, as inferred from the H–κ results (Fig. 3a).

To ensure that these split phases are not artefacts of stacking, we examined their backazimuthal and slowness dependence. For instance, station N058 displays a single, unsplit Pms phase (Fig. 6a), while stations N111 and N044 show clear Pms splitting in the 0°–180° range (Figs 6b and c), despite limited azimuthal coverage. Additional examples of stations showing split Pms in the eastern backazimuths, similar to N111, are presented in Fig. S5. Importantly, the split phases are evident even in individual (unstacked) RFs (Figs 6d and e). Slowness-domain plots for N111 and N044 (Figs 6d and e) reveal slightly diverging slopes, consistent with diffraction from a step-like Moho (Z. Yan & R.W. Clayton 2007), as schematically illustrated in Fig. 2(b).

Based on the spatial distribution and vertical extent of the offsets, we categorized the step-like features into two groups: a western offset group and an eastern offset group. Of the 32 stations exhibiting split Pms phases, 28 are associated with the western group (sky blue in Fig. 4a) and 4 with the eastern group (purple in Fig. 4a), reflecting the concentration of larger step-like features in the western part of the study region. The western group exhibits larger vertical offsets (∼5 km) and follows a NNE–SSW trend, consistent with fault strike trends of the JiF, MiRF, MoRF and YSF within the YFS. In contrast, the eastern group, located near the USF, shows smaller vertical offsets of ∼2 km. The smaller offset is associated with less pronounced Pms splitting, often appearing as a broadened pulse rather than two distinct arrivals (Fig. 6e).

Stations exhibiting split Pms phases were excluded from the H–κ stacking and crustal anisotropy analyses (open squares in Figs 3a and 7a). Because split Pms phases do not show a single, well-defined arrival, reliable Pms timing is difficult to obtain and the timing of associated multiples can also be affected (Fig. S5). Additional details are provided in Figs S6, S7, S8 and Text S1.

4.4. 2-D synthetic tests for split Pms phases associated with a step-like Moho

The spatially localized occurrence of split Pms phases, observed at only a subset of stations, suggests lateral variations in Moho depth. Motivated by the diffraction-like characteristics observed in eastern backazimuth RFs, we now assess the interpretation of the split Pms phases using the 2-D synthetic modelling.

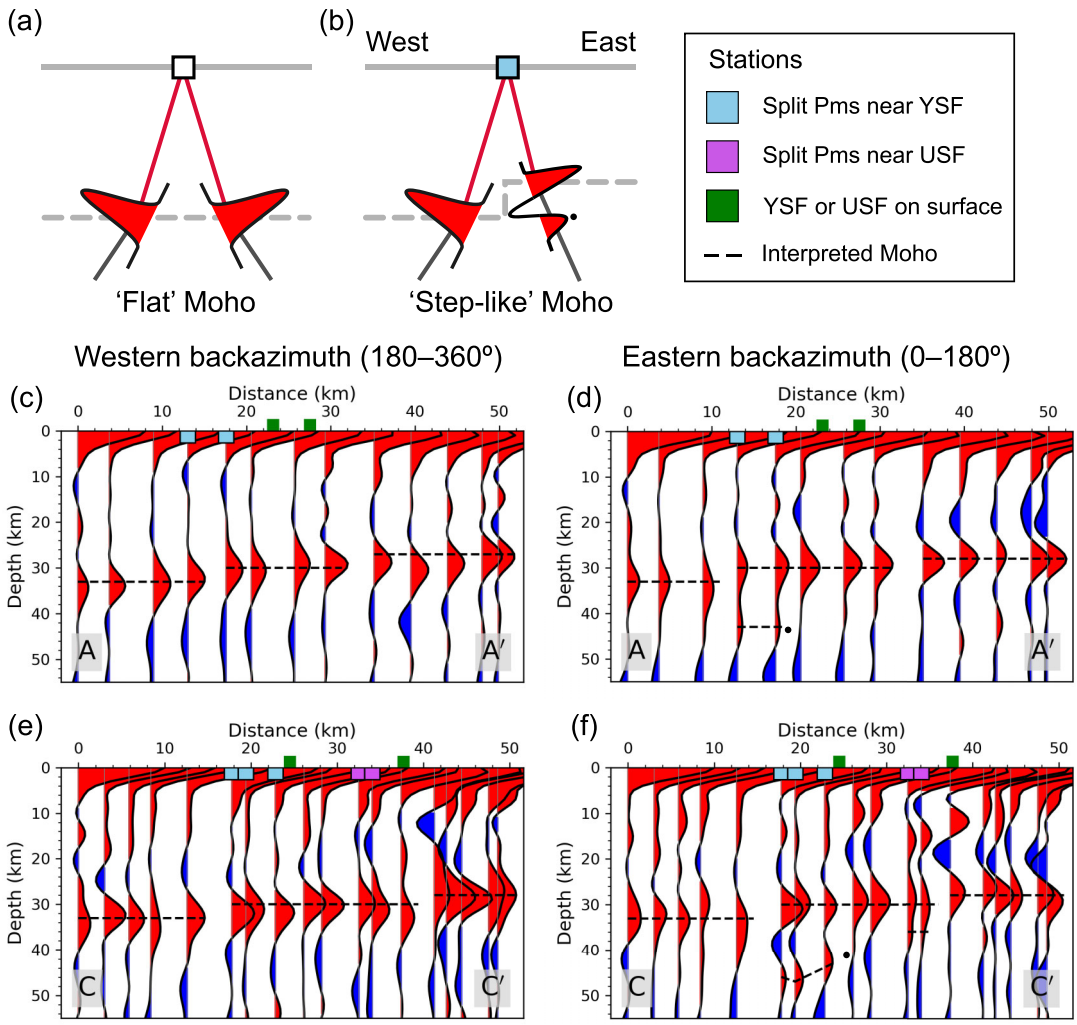

Figure 5. Station-stacked radial RFs stacked in two different backazimuth ranges. (a) Flat Moho characterized by a single Pms arrival with no directional dependence. (b) Step-like Moho, showing a single Pms on the western (deeper) side and split Pms on the eastern (shallower) side. (c, d) Radial RFs stacked from stations along profile A–A′: (c) for western backazimuths (180°–360°), (d) for eastern backazimuths (0°–180°). (e, f) Same as (c, d), but for profile C–C′. The black dot indicates the second phase of the split Pms, interpreted as a diffracted phase generated at the sharp Moho step. Other symbols are consistent with those in Fig. 4.

4.4.1. *Origin of split Pms phases*

A step-like Moho geometry is proposed as the primary origin of the split Pms phases; however, the potential contribution of alternative mechanisms also needs to be evaluated. To assess the origin of the secondary arrival, we conducted a series of 2-D synthetic tests for (1) fault-zone scattering (Fig. S9 and Text S2, M.A. Lewis & Y. Ben-Zion 2010), (2) shallow reverberations (Text S3) and (3) crustal anisotropy (Text S4) as potential alternative explanations. None of these models reproduced the observed backazimuth-dependent Pms splitting, supporting our interpretation of a step-like Moho geometry.

4.4.2. *Frequency dependence of split Pms resolution*

Wavefield simulations show that the incident *P* wave exhibits different propagation patterns in the flat-Moho and step-Moho models. In the flat-Moho model, the plane *P* wave is partitioned into transmitted and reflected waves at the Moho without geometric distortion (Fig. 8a). In contrast, the Moho-offset model produces concentric distortion patterns around the step due to diffraction at the Moho offset (Fig. 8b), which appear in the RFs as split Pms phases.

Because the detectability of the secondary arrival in the split Pms depends on both the step height and the frequency content of the RFs, we evaluated the conditions under which the split Pms phase becomes resolvable. We tested step heights from 1 to 6 km (1-km increment) by fixing the western Moho depth at 35 km (Fig. 8c).

Synthetic RFs were computed at a station located directly above the step (slowness of 0.06 s km^{-1}; incident angle of 20.4°), using the same model parameters as in Fig. 2(b). Under the filtering conditions used in this study (0.05–1.0 Hz bandpass filter; Gaussian filter width of 2.5), a ∼5-km step produces two resolvable Pms arrivals, whereas a 2-km step does not. This indicates that the western Moho offset, where split Pms phases are predominantly detected, is likely on the order of 5 km, whereas smaller offsets (∼2 km) tend to produce Pms phases that are not clearly separated into two independent peaks. Additional tests of the Gaussian filter widths are provided in Text S5 and Fig. S10.

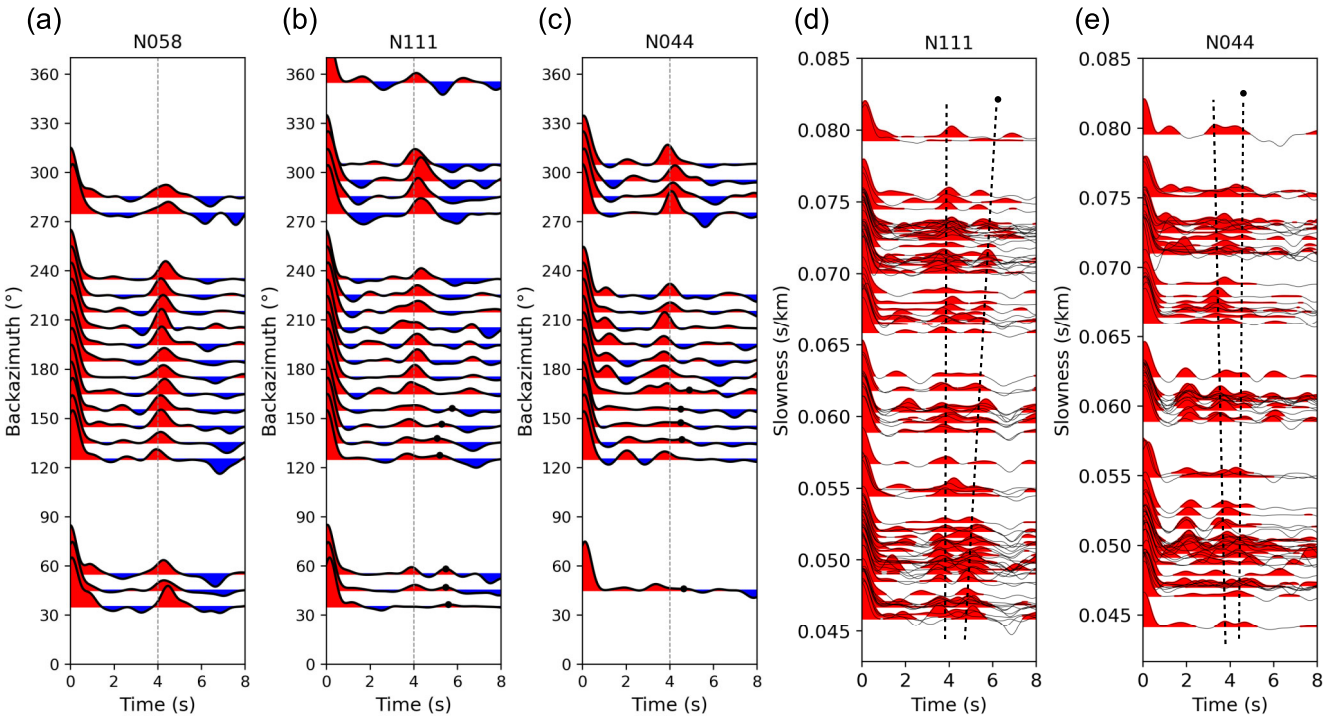

Figure 6. Pms phases near 4 s in the radial RFs at stations N058, N111 and N044. The station locations are shown in Fig. 4(a). (a) RFs at station N058, showing a single Pms. (b, c) RFs at stations N111 and N044, respectively, both showing split Pms arrivals. The RFs in (a), (b) and (c) are stacked using 10° backazimuth bins. (d, e) Non-stacked RFs at stations N111 and N044, respectively, for events from eastern backazimuth (0°–180°), sorted by slowness. Black dots in (b), (c), (d) and (e) indicate the second phase of split Pms arrivals, interpreted as diffracted phases from Moho offsets. Stations N111 and N044 are located near the YSF and USF, respectively.

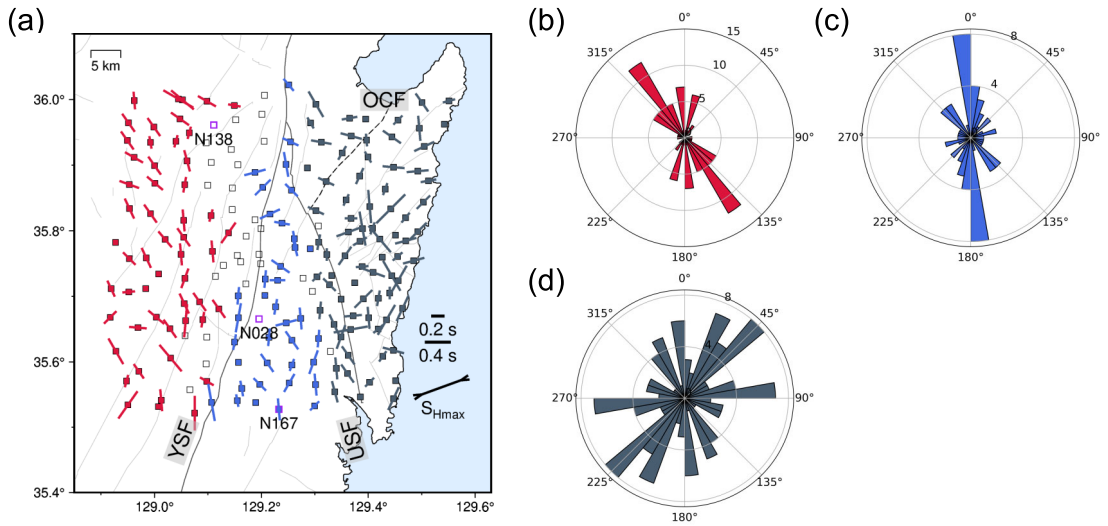

Figure 7. Spatial distribution of FSA and δt. (a) Anisotropy measurements at selected stations. Bars represent the azimuth of the FSA and their lengths indicate the δt. Measurements in Region 1, Region 2 and Region 3 are shown in red, blue and grey, respectively. Black open squares mark stations with split Pms phases, interpreted as locations of Moho offsets. Squares with no anisotropy measurements exhibit JOF values less than 1.1 and δt less than 0.05 s. (b–d) Rose diagrams of FSA for (b) Region 1, (c) Region 2 and (d) Region 3. Radial axis indicates the number of measurements in each azimuth bin. An example of joint analysis of radial and tangential RFs at station N167 is shown in Fig. S10 with optimal values of FSA = 175° and δt = 0.35 s. Additional examples from stations N138 and N128, which exhibit split Pms phases and were not used for interpretation, are presented in Fig. S11.

4.4.3. Slowness effects on the second peak amplitude of the split Pms phase

In synthetic tests, we found that the second peak (A_2) of the split Pms phase exceeds the first peak (A_1) under specific conditions. This behaviour occurs only at stations located west of the Moho offset and for low-slowness cases (< 0.060 s km^{-1}; Fig. 8d). Using a 5-km Moho offset model, synthetic RFs computed at representative sites—located 2 km west (Fig. 8d) and 2 km east (Fig. 8e) of the step—confirm that $A_2 > A_1$ is restricted to the western side of the step (Fig. 8d), whereas stations east of the step consistently exhibit $A_1 > A_2$ (Fig. 8e).

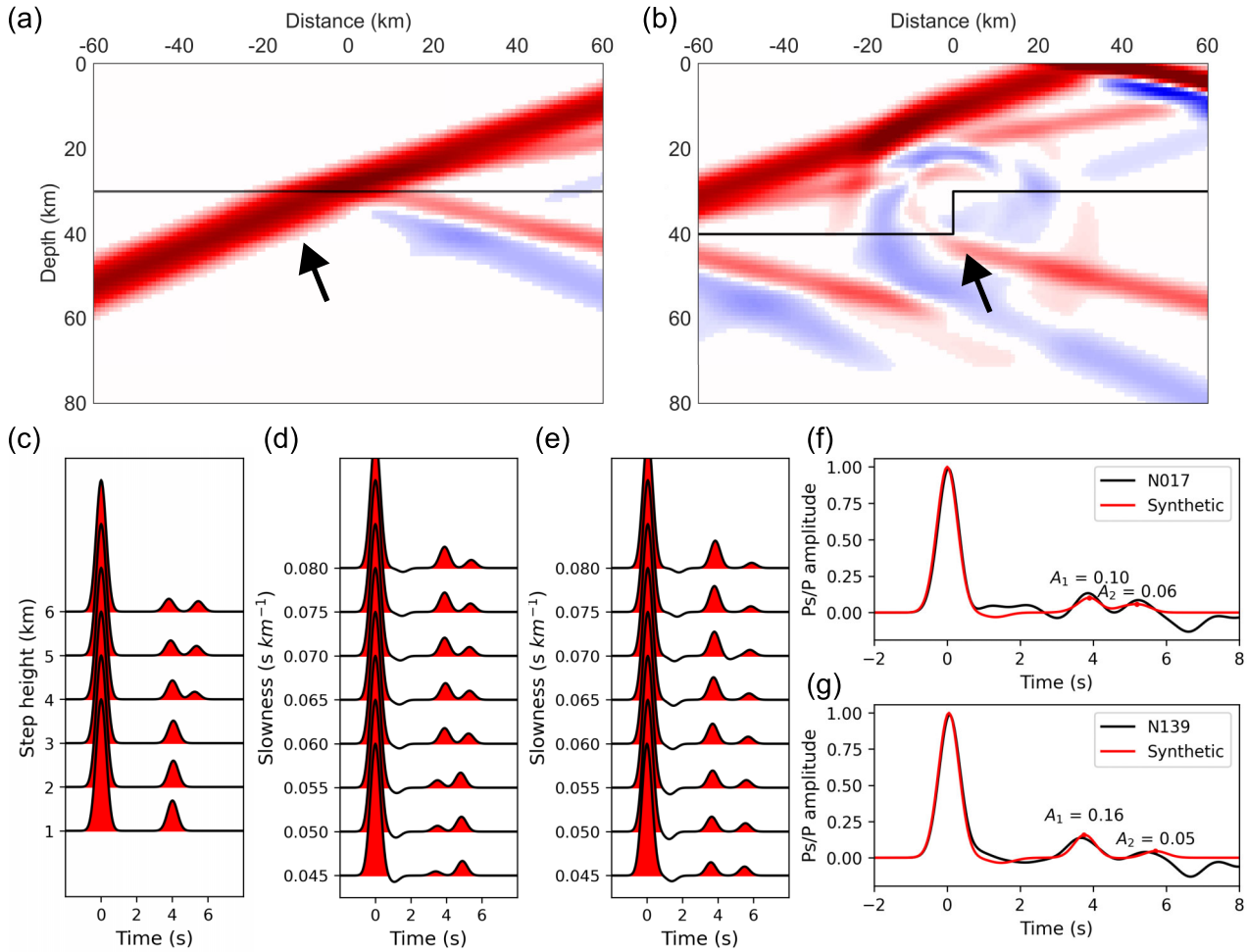

Figure 8. 2-D modelling of split Pms phases. (a, b) Snapshot of plane *P*-wave propagation for a flat Moho at a depth of 30 km (Fig. 2a) and a step Moho model (Fig. 2b), respectively. Black lines indicate the Moho geometry in each panel. Red and blue colours denote positive and negative polarities in the radial component. Black arrows indicate the directions of the incident plane *P* waves. (c) Synthetic RFs computed for step heights ranging from 1 to 5 km with Gaussian filter width of 2.50. (d, e) Synthetic RFs computed at a station located 2 km west and 2 km east of the step, respectively, for slowness values of 0.045–0.080 s km^{-1} in increments of 0.005 s km^{-1}. The synthetic RFs were generated using a model where the Moho shallows eastward from 33 to 28 km. (f, g) Comparison between observed and synthetic RFs for stations N017 and N139, respectively. The observed RFs are stacked using only eastern-backazimuth events, and the synthetic RFs are obtained by stacking the RFs in panels (d) and (e). All synthetic RFs are generated using the model parameters shown in Fig. 2(b). A_1 and A_2 of the stacked synthetic RFs in (f) and (g) are labelled.

We then examined whether this pattern is also present in the observed RFs. Several stations indeed show a clear increase in the proportion of traces with $A_2 > A_1$ at low slowness. To assess statistical significance, we performed a one-sided *z*-test at a significant level of 0.05 to compare the proportions of $A_2 > A_1$ between the low- and high-slowness groups. These stations are predominantly located west of the YSF (Fig. 3a, red squares), consistent with the synthetic prediction that the Moho offset lies to the east of these stations (Fig. 3a; Text S6).

Although the synthetic tests predict $A_2 > A_1$ for all low-slowness cases on the western side of the step, many observed RFs still show $A_1 > A_2$ (Figs S11b, d and f). We attribute this to the effect of 3-D structural complexities not captured by our simplified 2-D model. Nevertheless, the statistically significant enhancement of A_2 at low slowness indicates that the key amplitude behaviour predicted by the synthetics is also present in the data (Fig. S11).

4.4.4. Amplitude and arrival-time comparison between observed and synthetic receiver functions

We stacked the synthetic RFs, normalized by the direct *P* amplitude, as shown in Figs 8(d) and (e), and compared these with two representative observed RFs: one from a station exhibiting $A_2 > A_1$ at low slowness (Fig. 8f) and the other that does not (Fig. 8g). In both synthetic and observed stacks, the second peak appears weaker because stacking mixes traces with different slowness values and slowness-dependent moveout of the second peak leads to a reduction in A_2.

We also note that the characteristics of the split Pms phases in the synthetic RFs differ systematically across the step. Western station shows smaller amplitude contrasts between A_1 and A_2 and a shorter time separation between the two peaks (Fig. 8d), whereas eastern station exhibits larger amplitude differences and a wider separation (Fig. 8e). We therefore assessed whether this synthetic west–east contrast is likewise reflected in the observed RFs.

For station N017 (location shown in Fig. 3a), the observed RF exhibits $A_2 > A_1$ at low slowness (Figs S11a and b), and the synthetic RF computed for the western station reproduces both the arrival times and amplitudes ($A_1 = 0.10$; $A_2 = 0.06$) with high consistency (Fig. 8f). This agreement suggests that N017 is likely located on the western side of the Moho step. In contrast, station N139 (Fig. 3a) does not exhibit $A_2 > A_1$ at low slowness, and its observed RF closely matches the synthetic RF generated for the eastern station in both timing and amplitude ($A_1 = 0.16$; $A_2 = 0.05$; Fig. 8g). This suggests that N139 is more plausibly located on the eastern side of the Moho offset.

Taken together, the observed and synthetic RFs imply that a ∼5-km Moho-offset geometry provides a coherent explanation for the spatial patterns across the study area. Although a few stations deviate from this behaviour, such variability is expected given the 3-D structural complexities that are not represented in our simplified 2-D model.

4.5. Crustal anisotropy

For interpretation, we divided the study area into three regions. We applied linear fitting to the two station groups described in Section 4.3—the western and eastern offset groups (Fig. 4a)—to define the boundaries (Fig. S12). These boundary lines, aligned NNE–SSW and NNW–SSE respectively, roughly follow the trends of the YSF and USF. Region 1 (Fig. 7a, red) lies west of the YSF, encompassing the JiF, MiRF and MoRF. Region 3 (grey) is east of the USF, including the YB and complex fault systems. Region 2 (blue) is the wedge-shaped block between the YSF and USF.

Anisotropy results are summarized in Fig. 7(a), where bar orientation and length represent FSA and δt, respectively. In Region 1, FSAs predominantly trend NW–SE (∼150°), particularly in the northwestern and southern areas (Fig. 7b). In Region 2, FSAs exhibit a N–S trend (175°) near the western side of the USF (Fig. 7c). Region 3 shows more scattered FSA directions, generally trending NE–SW to E–W (45°–90°), with relatively larger δt values (>0.4 s) near 35.6°N–35.9°N and smaller values northwest of the Ocheon Fault (OCF) (Fig. 7d). Average δt values are similar across the three regions: 0.33 s (Region 1), 0.30 s (Region 2) and 0.32 s (Region 3) (Fig. S14). While FSAs show clear spatial variation, δt does not vary significantly between regions.

5 DISCUSSION

5.1. Two-step-like Moho geometry

Our RF results reveal a two-step Moho geometry beneath the southeastern Korean Peninsula, characterized by two distinct vertical offsets. These offsets are spatially correlated with major faults, suggesting their formation through fault movement and reactivation under evolving tectonic regimes. Such stepped structures provide valuable insights into the mechanisms by which passive continental margins record and respond to major tectonic events, particularly those involving a transition from tensional to compressional stress regimes. However, these step-like features are not well resolved in the H–κ stacking method (Fig. 3a), which assumes a locally flat Moho and averages over an effective radius of ∼8 km. This broad spatial window—combined with the use of distance- and uncertainty-based weighting factors—results in smoothing of the results. In contrast, station-based stacking, with ∼4.5 km average spacing, offers higher spatial resolution and better captures localized Moho offsets.

5.1.1. *Inferred Moho geometry from 2-D modelling*

To investigate how the Moho offsets affect the spatial distribution of diffracted Pms phases, we conducted 2-D synthetic waveform modelling (T. Maeda *et al.* 2017). We assumed three different geometries (Figs 9a, c and e), and corresponding synthetic RFs calculated from eastern backazimuths are shown in Figs 9(b), (d) and (f), respectively. The synthetic RFs for western backazimuths computed using the same geometries are provided in Fig. S15.

In all models, a common vertical Moho offset on the eastern side was implemented as a sharp depth change from 28 to 26 km at a horizontal distance of 10 km (Figs 9a, c and e). The western Moho offset varies by model: a vertical step from 33 to 28 km at −10 km (Fig. 9a), an oblique ramp from 33 to 28 km (Fig. 9c) and a gently dipping ramp from 33 to 28 km (Fig. 9e). The crustal and mantle properties were the same as those shown in Fig. 2(b). The computational grid spacing was 0.2 km in both horizontal and vertical directions. Synthetic waveforms were recorded at virtual stations spaced at 1 km intervals along the surface. For all simulations, we assumed an incident *P* wave with a fixed angle of 19°, corresponding to a slowness of 0.056 s km^{-1} from the east.

The vertical step model (Figs 9a and b) produced diffracted phases confined within a radius of ∼2.5 km of the western step, which is consistent with observations from the central and southern parts of the study region. In these areas, stations showing split Pms phases are concentrated within ∼5 km of the Moho offset, suggesting a steep, near-vertical step geometry. The oblique-ramp model (Figs 9c and d) generates a broader distribution of diffracted phases around the western offset, extending up to ∼10 km. This model better explains observations in the northern part of the study area (Fig. 3a; open squares with an overlaid cross), where split Pms phases are detected up to ∼10 km from the Moho step. Lastly, the dipping ramp model (Figs 9e and f) produces little diffracted energy, suggesting that such a gradual Moho transition is inconsistent with our observations. In all models, the eastern vertical step with a small offset yields weaker diffracted phases (Figs 9b, d and f), consistent with the observations. When combined with the RF stacking results, the 2-D modelling provides a detailed characterization of Moho geometry, highlighting its spatial variability and structural complexity beneath our study region.

5.1.2. *The western Moho offset*

A distinct Moho offset is observed along the YFS in the GB (Fig. 4a). The YSF, the major structure within the YFS, experienced both left-lateral and right-lateral strike-slip movements due to changes in palaeo-stress regimes. During the Late Cretaceous to early Cenozoic, NW–SE compressional stress induced left-lateral strike-slip motion (H. Cho *et al.* 2016). Subsequently, during the Eocene to Oligocene, NE–SW compression resulted in right-lateral strike-slip movement (Fig. 10a). This later phase of deformation overprinted the earlier left-lateral system (Y. Cheon *et al.* 2019, 2020), resulting in the present-day ∼20–30 km horizontal offset observed along the fault (B.H. Hwang *et al.*

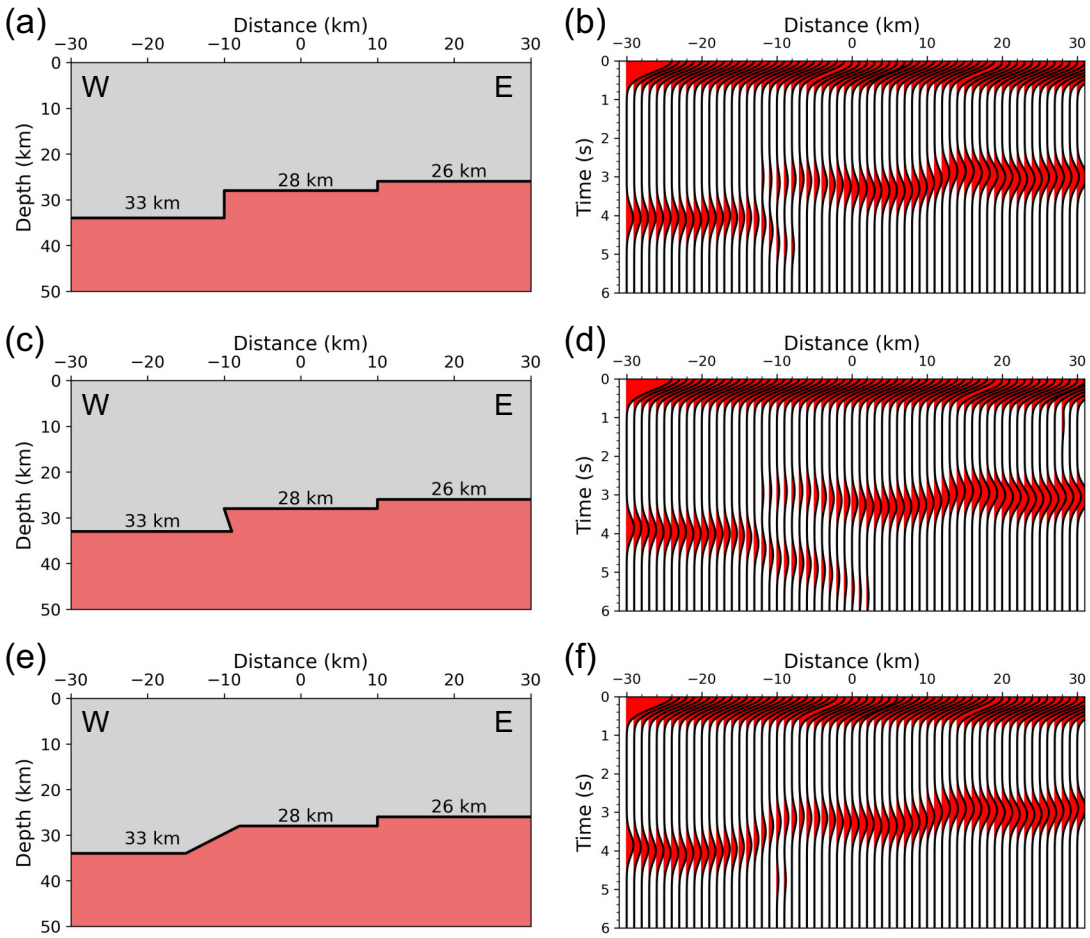

Figure 9. 2-D modelling results for different Moho geometries. (a, c, e) Three Moho offset models: (a) vertical Moho, (c) oblique ramp Moho and (e) dipping ramp Moho. Upper layers represent the crust, and lower layers represent the mantle. All models use the same velocity model in Fig. 2(b). Moho offsets are located at horizontal distances of −10 and 10 km, where the Moho depth changes sharply from 33 to 28 km, and from 28 to 26 km, respectively. (b, d, f) Synthetic radial RFs calculated from eastern backazimuths for the corresponding models: (b) vertical Moho, (d) oblique ramp Moho and (f) dipping ramp Moho.

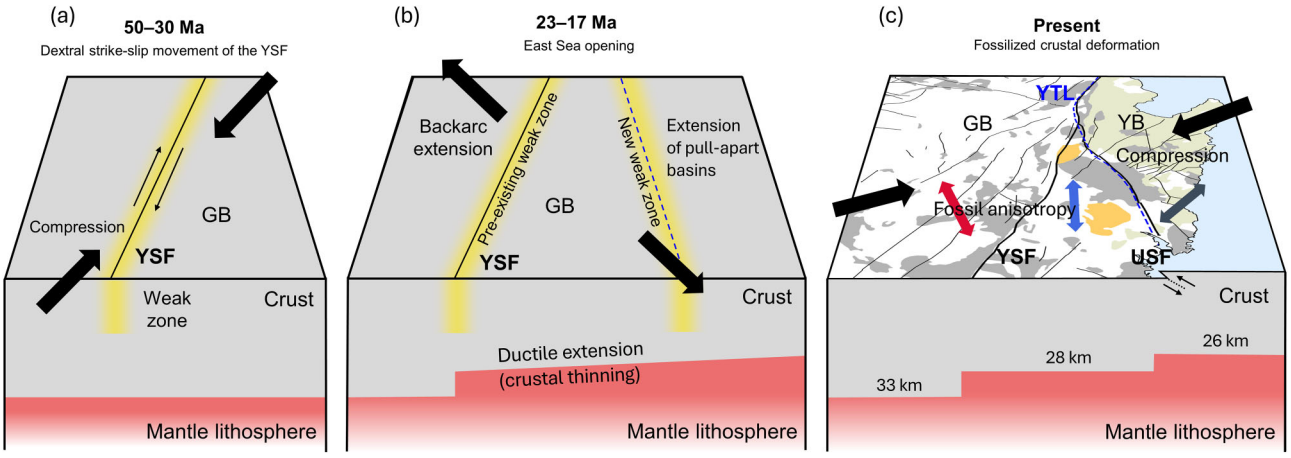

Figure 10. Schematic diagrams illustrating the tectonic evolution and associated Moho offset deformation. (a) Dextral strike-slip movement along the NNE–SSW striking YSF under NE–SW compressional stress, producing a 20–30 km offset and forming a crustal weak zone. (b) During the backarc opening, oblique extension was localized along this pre-existing weak zone, inducing ductile deformation and generating the Moho offset near the YFS. Small pull-apart basins and eastwards crustal thinning also developed. (c) Following the East Sea opening, compressional reactivation of the weak zone formed a thrust fault along the USF. Passive mantle upwelling and uplift near the USF led to an additional Moho offset. Coloured arrows show the directions of crustal anisotropy in Region 1, Region 2 and Region 3.

2007, 2008; Y. Cheon *et al.* 2019, 2020). Such long-term strike-slip faulting is known to promote the development of weak zones through strain localization (Y. Finzi *et al.* 2011), grain-size reduction (C.G. Sammis & Y. Ben-Zion 2008), and hydrothermal alteration along fault cores (D.R. Faulkner *et al.* 2010; B. Marchesini *et al.* 2025). Drill-core analyses from the YSF support this, revealing fluid-assisted alteration and hydrothermal reactions that weakened the fault core (C.M. Kim *et al.* 2022).

The tectonic regime later transitioned from compression to tension, due to the initiation of slab rollback of the Pacific Plate during large-scale backarc extension, resulting in NW–SE-oriented extension, which is oblique to the NNE–SSW-striking YSF (Y.-I. Otofuji & T. Matsuda 1983; S. Lallemand & L. Jolivet 1986; M. Son *et al.* 2015). Such oblique extension enhanced ductile deformation and concentrated stress on the pre-existing weak zones (S. Brune *et al.* 2012), facilitating ∼5 km Moho depth changes along the YFS (Fig. 10b). A notable Bouguer anomaly contrast across the YSF (S. Choi *et al.* 2023) is generally consistent with the presence of the Moho offset observed in this study.

Oblique extension does not necessarily lead to normal faulting. When the extension direction is oriented closer to the strike of a pre-existing weak zone than to its normal, shear deformation can become dominant, focusing strain along the central portion of the weak zone (M.O. Withjack & W.R. Jamison 1986; A. Agostini *et al.* 2009; S. Brune *et al.* 2012). In this context, shear localization along the YSF could have contributed to the development of the observed Moho offset, although this mechanism cannot be uniquely confirmed. This interpretation is supported by the absence of clear geological evidence for significant Miocene normal-slip displacement along the YSF, including the lack of adjacent Miocene basin fills (Y. Cheon *et al.* 2019). In addition, the steep dip of the YSF ($>80^{\circ}$) suggests that any extensional component during oblique extension would have been limited. Accordingly, while we cannot fully rule out other processes, normal faulting alone appears unlikely to account for the Moho offset near the YSF.

5.1.3. The eastern Moho offset

The eastern Moho offset is located adjacent to the western boundary of the YB, which underwent clockwise rotation during the backarc opening (M. Son *et al.* 2015; A. Van Horne *et al.* 2017; Y. Cheon *et al.* 2023). During the backarc opening in the Miocene, the crust in this region underwent significant thinning of ∼7 km due to tensional stress (S. Park & T.K. Hong 2024), as indicated by the shallower Moho depth beneath the eastern margin (Fig. 3a). Following the cessation of the backarc opening, the regional stress regime inverted to compression. As a result, the weak zone formed during the backarc extension was reactivated as a low-angle thrust fault (Figs 10b and c), forming the present-day USF (J.-H. Ree *et al.* 2003; N. Kim *et al.* 2023; Y. Cheon *et al.* 2023). The vertical uplift of the YB, as the hanging wall of the USF, may have contributed to the uplift of the underlying Moho, resulting in the observed offset (Fig. 10c). This interpretation is further supported by a large Bouguer anomaly (>50 mGal) in the YB region (S. Choi *et al.* 2023), indicating the presence of uplifted, dense mantle material and an associated rise in Moho depth.

Our study identifies Moho offsets within the stable continental crust of the southeastern Korean Peninsula, far from any active plate boundary. While most studies in other regions have reported relatively large offsets (∼10 km) from teleseismic RF methods (Z. Yan & R.W. Clayton 2007; D. Shi *et al.* 2009; V. Schulte-Pelkum & Y. Ben-Zion 2012), the exceptionally dense station coverage of the GHBSN allowed us to detect smaller scale Moho offsets (2–5 km), providing unprecedented resolution of crustal structures in this passive margin setting. Such small-scale Moho structures, resolvable only by dense seismic arrays, offer valuable constraints for interpreting tectonic histories preserved in stable continental crust. Our findings thus provide a useful comparative framework for understanding lithospheric deformation and tectonic evolution beyond regions near active boundaries.

5.2. Crustal seismic anisotropy

Based on the observations of Moho offsets near the YFS, our crustal anisotropy measurements further highlight the complex interactions between fault movements and past tectonic events in the region. The dominant FSAs in Regions 1 and Region 2, oriented in NW–SE and N–S directions, respectively (Figs 7b and c), do not align with the present-day ENE–WSW maximum horizontal compressional stress (Y. Park *et al.* 2006; I. Soh *et al.* 2018). This discrepancy indicates that the observed FSAs are unlikely to represent stress-induced anisotropy, as such anisotropy typically develops parallel to the direction of maximum horizontal compressional stress (N.L. Boness & M.D. Zoback 2006). Instead, these patterns are better explained by fossil anisotropy, preserved from past tectonic regimes, particularly the shear stress associated with the backarc extension during the Miocene.

In Region 1, the NW–SE orientation of the dominant FSA is consistent with the tensional stress direction during the backarc extension (Y. Cheon *et al.* 2012, 2023; M. Son *et al.* 2015; X. Liu & D. Zhao 2016), suggesting that crustal deformation and mineral alignment from that period have been retained. In Region 2, the FSAs are oriented slightly clockwise relative to Region 1, likely reflecting the combined effects of fossil anisotropy and fault structure-related anisotropy, where mineral or crack alignment along fault zones has modified the anisotropic fabric (N.L. Boness & M.D. Zoback 2006). A similar interpretation has been proposed for the central North China Craton, particularly along the boundary between the northern Yanshan Uplift and the southern Bohai Bay Basin, where RF data revealed crustal anisotropy attributed to fossil fabrics formed during Mesozoic lithospheric extension (T. Zheng *et al.* 2019). Similar fossil anisotropy patterns associated with past rifting episodes have also been documented in other extended continental regions, such as the Somaliland rift basins, where RF-based measurements revealed anisotropic fabrics aligned with the Late Jurassic extension event (M.Y. Ali *et al.* 2023).

In contrast, Region 3 exhibits scattered FSAs (Fig. 7d), indicative of a more complex tectonic history. This region, predominantly composed of Miocene-aged rocks, was strongly influenced by magmatism, sedimentation and formation of pull-apart basins such as the Pohang Basin, which is bounded by the OCF (Y.K. Sohn 2000; Y. Cheon *et al.* 2012). The relatively younger lithology and complex fault structures likely disrupted the preservation of fossil anisotropy. The scattered anisotropy observed in this region appears to reflect the present maximum horizontal compressional stress direction and localized deformation (J.-H. Ree *et al.* 2003; Y. Park *et al.* 2006; I. Soh *et al.* 2018). These contrasting anisotropy patterns between regions

suggest that the GB and YB experienced different deformation behaviours during the backarc extension.

5.3. Average crustal V_P/V_S

The crustal V_P/V_S ratio is widely regarded as a proxy for crustal composition and physical properties. Rocks with higher silica content generally exhibit lower V_P/V_S, with felsic composition typically showing lower values and mafic rocks higher ones (N.I. Christensen 1996). In our study region, the average V_P/V_S ratio is 1.82, which exceeds the global continental average of 1.77 (N.I. Christensen & W.D. Mooney 1995), indicating mafic enrichment of the crust possibly associated with the Miocene backarc opening. Previous studies have also reported higher V_P/V_S in this region compared to other regions of the southern Korean Peninsula. For instance, S.J. Chang & C.E. Baag (2007) reported a crustal average of 1.81, while E. Jo & T.K. Hong (2013) attributed an upper crustal estimate of 1.75 to the presence of volcanic or volcaniclastic rocks.

In addition to the high average value, our high-density seismic network reveals localized variations in V_P/V_S ratios that further indicate crustal heterogeneity (Fig. 3b). Specifically, we identified two distinct anomalies: a low V_P/V_S anomaly ($<$1.73) and a high V_P/V_S anomaly ($>$1.85). A prominent low V_P/V_S anomaly is observed near the intersection of the YSF and USF, corresponding closely with a low-density zone identified in a previous gravity survey, attributed to the lower density of the granite compared to the surrounding sedimentary rocks (S. Choi *et al.* 2023). This low V_P/V_S value is consistent with laboratory-determined V_P/V_S values for felsic rocks such as granite, which typically range from 1.70 to 1.71 under crustal pressure conditions (N.I. Christensen 1996). Notably, the low V_P/V_S zone also encompasses the epicentral regions of the M_L 4.2 earthquake on 1997 June 26 (T.W. Chung & W.H. Kim 2000), and the M_W 5.5 earthquake on 2016 September 12 (Y. Kim *et al.* 2017)—the largest instrumentally recorded earthquake in the Korean Peninsula (Fig. 3b; labelled 1 to 4). These $M \geq 4$ events occurred within a region of low V_P/V_S, suggesting a relatively rigid crust that is more likely to accumulate elastic strain over time and release it through large-magnitude brittle failure (O. Katz & Z. Reches 2004; S. Zertani *et al.* 2025).

Conversely, elevated V_P/V_S anomalies in our study area may be attributed to several factors. First, high surface heat flow, particularly along the YFS, may thermally weaken the crust and reduce V_S (H.C. Kim & Y. Lee 2007; Y. Lee *et al.* 2010; H. Li *et al.* 2022). Secondly, complex fault structures and high fault density in certain areas can lead to pervasive fracturing, which also reduces V_S and elevates V_P/V_S values (P. Ding *et al.* 2019; K. Kim *et al.* 2023). Thirdly, mafic compositions, as evidenced by basaltic outcrops in the YB region (S.-H. Shim *et al.* 2011; H.O. Choi *et al.* 2013), may locally increase V_P/V_S ratios. These features likely reflect long-term modifications inherited from past tectonic processes, such as magmatism and backarc extension.

In our study region, two high V_P/V_S anomalies are identified: one near the MiRF and MoRF in the west of the YSF, and another within the YB (Fig. 3b). The western anomaly coincides with zones of elevated heat flow ($>$90 mW m^{-2}; H.C. Kim & Y. Lee 2007; Y. Lee *et al.* 2010) and fracture zones (K. Kim *et al.* 2023), both indicative of thermally and mechanically weakened crust. The YB anomaly corresponds to weak zones associated with the Miocene backarc extension and later reactivated under compressional stress (J.-H. Ree *et al.* 2003; K. Kim *et al.* 2023; Y. Cheon *et al.* 2023). This weakened crust may explain the concentration of microseismicity in this area (J.U. Woo *et al.* 2019; D. Heo *et al.* 2024). In addition, mafic lithologies exposed in the YB (S.-H. Shim *et al.* 2011; H.O. Choi *et al.* 2013) likely contribute to the elevated V_P/V_S values.

6 CONCLUSIONS

We conducted high-resolution P-RF imaging using the dense broad-band seismic network to investigate the crustal structure of the southeastern Korean Peninsula and its links to past tectonic events and present-day seismicity. Our results reveal two distinct Moho offsets associated with Miocene backarc extension and subsequent fault reactivation, highlighting significant lateral variability in the crust. Crustal anisotropy shows spatially heterogeneous patterns: fossil anisotropy aligned with past tensional stress is preserved in the older Gyeongsang Basin, while the younger Yeonil Basin exhibits a combination of fossil and present-day stress-induced anisotropy. Spatial variations in V_P/V_S ratios further indicate compositional heterogeneity and fault-related fracturing, with low V_P/V_S zones corresponding to relatively rigid crust where $M \geq 4$ earthquakes are concentrated, and high V_P/V_S anomalies associated with mechanically weakened regions hosting microseismicity. Taken together, these observations demonstrate that extension-related deformation and inherited heterogeneity are preserved in the crust of this fossil backarc system, imprinting a structural and mechanical framework that governs the distribution and occurrence of present-day earthquakes.

SUPPORTING INFORMATION

Supplementary data are available at *GJI* online.

Figure S1. Change in sensor misorientation at station N009 (a) RFs calculated using previously reported misorientation angles for each time window (M.-S. Seo *et al.* 2022). After 2022, the tangential RFs show larger amplitudes than the radial RFs at *P*-wave arrivals, suggesting a possible change in sensor orientation. (b) RFs recalculated after applying an updated orientation correction, estimated by a teleseismic waveform-based grid search. The misorientation angle after 2022 is estimated as 66.4°. (c) Summary table showing temporal changes in misorientation angles at station N009.

Figure S2. Synthetic radial and tangential RFs for isotropic and anisotropic crust models. (a) Radial and tangential RFs for the isotropic crust. The Pms phase appears at 3.8 s on the radial RFs with no variation in lagtime, while the tangential RFs show no energy. (b) Synthetic RFs for an anisotropic crust model, constructed by introducing a fast symmetric axis (FSA) oriented at 0° azimuth and a peak-to-peak anisotropic strength of 6 per cent to the isotropic model shown in Fig. 2(b). (c) Inversion results for the anisotropic models in (b), showing optimal estimates of FSA azimuth and delay time (δt) based on four objective functions defined in H. Liu & F. Niu (2012): 'max(RCOS)', 'max(RCC)', 'min(T energy)' and 'JOF'. The white symbol 'x' indicates the optimal combination of FSA and δt.

Figure S3. Examples of H–κ stacking results for stations N051 and N117. (a) Estimates of H (33.3$\pm$1.0 km) and κ (1.76 $\pm$0.03) at station N051. (b) Estimates for station N117 (H = 27.8 $\pm$1.3 km;

$\kappa = 1.80 \pm 0.05$). (c) Lagtimes of the Pms, PpPs, and PpSs + PsPs phases calculated from the H and κ on the radial RFs at station N051. Black lines represent uncertainties in the optimal Moho depth and κ (or V_P/V_S). (d) Same as (c), but for station N117. t_1, t_2 and t_3 indicate arrival times of Pms, PpPs and PpSs + PsPs phases, respectively. Station locations are shown in Fig. 3(a).

Figure S4. Station-stacked radial RFs for different backazimuth ranges along profiles B–B′ and D–D′. (a, b) RFs stacked from western and eastern backazimuths, respectively, along profile B–B′. (c, d) Same as (a, b), but for profile D–D′. Symbols are consistent with those used in Figs 4 and 5.

Figure S5. Additional examples of split Pms phases at stations showing similar patterns to N111 (Fig. 6b). (a–d) Backazimuth-binned stacked RFs at stations N006, N013, N012 and N028, respectively. All stations show clear split Pms phases. Dots indicate diffraction phases, consistent with those shown in Fig. 5(b). These stations are located near the YFS, and the observed split Pms phases are interpreted as diffraction generated by sharp Moho offsets.

Figure S6. H–κ stacking result for 1-D synthetic RFs. (a) Velocity model used in the calculation. The Moho depth, average crustal V_P and V_P/V_S were assumed to be 30 km, 6.3 km s^{-1} and 1.73, respectively. (b) Synthetic RFs sorted by slowness. (c) H–κ stacking results obtained from the RFs shown in (b).

Figure S7. H–κ stacking results for 2-D synthetic RFs generated by an eastern-incidence plane wave. (a) Velocity model. The Moho depth, average crustal V_P and V_P/V_S were assumed to be 30 km, 6.3 km s^{-1} and 1.73, respectively. (b) Synthetic RFs sorted by slowness. (c) H–κ stacking results obtained from the RFs shown in (b).

Figure S8. Crustal anisotropy measurements from the joint analysis of radial and tangential RFs at stations (a) N138 and (b) N028, which show split Pms phases.

Figure S9. Synthetic RFs for the model including a fault fracture zone. (a) Velocity model used for the calculation. (b) Synthetic RFs for western-incidence plane waves. (c) Synthetic RFs for eastern-incidence plane waves. All synthetic RFs were calculated for a slowness of 0.050 s km^{-1}.

Figure S10. Synthetic RFs for different step heights and Gaussian filter widths (GFWs). For the step heights of 1–6 km, the GFW was varied as (a) 4.0, (b) 3.5, (c) 3.0, (d) 2.5, (e) 2.0 and (f) 1.5.

Figure S11. Observed RFs and statistical analysis of amplitude ratios. (a, c, e) RFs observed at stations N017, N138 and N038, respectively. Synthetic RF is the stack of the synthetic RFs shown in Fig. 8(d). Blue histograms indicate the number of RFs in each slowness bin for eastward backazimuths, while orange histograms show those satisfying $A_2 > A_1$. (b, d, f) correspond to stations N017, N138 and N038, respectively, with the proportions of traces exhibiting $A_2 > A_1$ at low (< 0.060 s km^{-1}) and high (≥ 0.060 s km^{-1}) slowness, annotated above each plot. (g) Observed RF at station N139 which does not satisfy $A_2 > A_1$, and the stacked synthetic RF shown in Fig. 8(e). All stacked synthetic RFs are normalized by the direct-*P* amplitude before stacking. (h) Spatial distribution of stations showing a statistically significant enhancement of A_2 at low slowness (p-value < 0.05), marked by squares with bold outlines. Colours indicate the p-values obtained from the z-test at each station.

Figure S12. Linear-fit boundaries separating station groups. The two solid lines delineate linear-fit boundaries that separate the western, central and eastern station groups used for the crustal anisotropy analysis. Open squares indicate stations excluded from the anisotropy measurements. Station symbols follow the conventions in Fig. 7.

Figure S13. Anisotropic inversion results from station N167 (Fig. 7a). (a–d) Inversion results for the azimuth of FSA and δt using the following schemes: (a) 'max(RCOS)', (b) 'max(RCC)', (c) 'min(T energy)' and (d) 'JOF'. Polar plots display the FSA as the azimuthal coordinates (in degrees) and δt as the radial coordinates (in seconds). The optimal values (FSA = 175°, δt = 0.35 s) are marked with a white 'x'. (e) Radial RFs. Dotted lines indicate Pms arrival times, calculated from synthetic RFs generated using the velocity model in Fig. 2(b) and the optimal anisotropic parameters from (d). (f) Tangential RFs. Black 'x' symbols indicate polarity reversal nodes derived from synthetic RFs based on the same anisotropic parameters and velocity model.

Figure S14. Delay time distributions for (a) Region 1, (b) Region 2 and (c) Region 3. Histograms are plotted with a bin size of 0.1 s. Black lines indicate average delay times for each region, calculated as 0.33, 0.30 and 0.32 s, respectively. Colour schemes for each region correspond to that used in Fig. 7.

Figure S15. 2-D modelling results for three Moho geometries: (a) vertical Moho, (c) oblique ramp and (e) dipping ramp. Upper and lower layers represent crust and mantle, respectively. All models use the same velocity structure as in Fig. 2(b). Moho offsets are located at horizontal distances of −10 and 10 km, where the Moho depth changes sharply from 33 to 28 km, and from 28 to 26 km, respectively. (b, d, f) Synthetic radial RFs calculated for western backazimuths for the corresponding models: (b) vertical Moho, (d) oblique-ramp Moho and (f) dipping-ramp Moho.

Table S1. Station information of the GHBSN used in this study. The table lists the station codes, operational periods, locations and elevations of the broad-band seismic stations. Latitude and longitude are provided in decimal degrees. The information reflects the station status as of 2024.

Table S2. List of six stations with misorientation angle changes exceeding 20° relative to previously reported orientation estimates (M.-S. Seo *et al.* 2022). The 'Valid From' column indicates the earliest date from which corrected orientations were applied. Because the estimates are based on a teleseismic waveform method, each correction was applied following the occurrence of a teleseismic event ($M_W \geq 5.8$); therefore, the listed dates may differ from the actual onset of misorientation changes. The corrected orientation values were used in RF calculations up to October 2023.

ACKNOWLEDGMENTS

This work was supported by the Nuclear Safety Research Program through the Korea Foundation of Nuclear Safety (KoFONS) using financial resources granted by the Nuclear Safety and Security Commission (NSSC) of the Republic of Korea (No. 1705010). MK and YK acknowledge the support by the NRF grant (MSIT) (No. RS-2022-NR070842 and RS-2022-NR069023). We are grateful to the GHBSN team from Seoul National University, Korea University, Pukyong National University, Pusan National University and Korea Institute of Nuclear Safety for installing and operating the GHBSN from 2017 to 2021. Lastly, we thank Editor Carl Tape, Xin Wang (Institute of Geology

and Geophysics, Chinese Academy of Sciences), and an anonymous reviewer for helpful comments that greatly improved the manuscript.

DATA AVAILABILITY

Raw data and receiver functions are available in Zenodo, at https://doi.org/10.5281/zenodo.15726512 (M. Kim, H. Lim & Y. Kim. 2025). Data pre-processing was conducted using Seismic Analysis Code (SAC) (https://ds.iris.edu/ds/nodes/dmc/software/downloads/sac/), and ObsPy (https://github.com/obspy/obspy). We used SeisPy for calculating and processing receiver functions (M. Xu & J. He 2022; https://github.com/xumi1993/seispy). Figures were created using Matplotlib (J.D. Hunter *et al.* 2007; https://github.com/matplotlib/matplotlib). Maps were created through PyGMT (P. Wessel *et al.* 2019; D. Tian *et al.* 2024; https://github.com/GenericMappingTools/pygmt). Synthetic receiver functions were generated using Raysum (https://home.cc.umanitoba.ca/~frederik/Software/) for the 1-D velocity model, and OpenSWPC (https://github.com/OpenSWPC/OpenSWPC) for the 2-D velocity model. The lithology information was derived from the 1:1000 000-scale Geological Map of Korea (W.-S. Kee *et al.* 2019; https://data.kigam.re.kr/data/d1a66b54-0541-4830-9b7f-0ea847430643?lang=en), and the fault and geological boundary datasets were obtained from the 1:250,000-scale Digital Geological Map of Korea (J.-C. Kim *et al.* 2002 ;https://data.kigam.re.kr/data/ac9b5c66-1768-447a-b28d-0eb0111ea401?lang=en), both provided by the Korea Institute of Geoscience and Mineral Resources (KIGAM).

REFERENCES

Agostini, A., Corti, G., Zeoli, A. & Mulugeta, G. 2009, Evolution, pattern, and partitioning of deformation during oblique continental rifting: inferences from lithospheric-scale centrifuge models, *Geochem. Geophys. Geosyst.,* **10**(11), doi:.

Ali, M.Y., Ismaiel, M., Yusuf, I.M. & Kaviani, A., 2023. Crustal structure and seismic anisotropy of rift basins in Somaliland, *Sci. Rep.,* **13**(1), 22041.

Ammon, C.J., 1991. The isolation of receiver effects from teleseismic *P* waveforms, *Bull. seism. Soc. Am.,* **81**(6), 2504–2510.

Berteussen, K.-A., 1977. Moho depth determinations based on spectral-ratio analysis of NORSAR long-period *P* waves, *Phys. Earth planet. Inter.,* **15**(1), 13–27.

Beyreuther, M., Barsch, R., Krischer, L., Megies, T., Behr, Y. & Wassermann, J., 2010. ObsPy: a Python toolbox for seismology, *Seismol. Res. Lett.,* **81**(3), 530–533.

Boness, N.L. & Zoback, M.D., 2006. Mapping stress and structurally controlled crustal shear velocity anisotropy in California, *Geology,* **34**(10), 825–828.

Brune, S., Popov, A.A. & Sobolev, S.V., 2012. Modelling suggests that oblique extension facilitates rifting and continental break-up, *J. geophys. Res.,* **117**(B8), B08402.

Chang, S.J. & Baag, C.E., 2006. Crustal structure in southern Korea from joint analysis of regional broadband waveforms and travel times, *Bull. seism. Soc. Am.,* **96**(3), 856–870.

Chang, S.J. & Baag, C.E., 2007. Moho depth and crustal vp/vs variation in southern Korea from teleseismic receiver functions: implication for tectonic affinity between the Korean Peninsula and China, *Bull. seism. Soc. Am.,* **97**(5), 1621–1631.

Cheon, Y. *et al.* 2023. Structural architecture and late cenozoic tectonic evolution of the Ulsan Fault Zone, SE Korea: new insights from integration of geological and geophysical data, *Front. Earth Sci.,* **11,** 1183329.

Cheon, Y., Cho, H., Ha, S., Kang, H.C., Kim, J.S. & Son, M., 2019. Tectonically controlled multiple stages of deformation along the Yangsan Fault Zone, SE Korea, since late Cretaceous, *J. Asian Earth Sci.,* **170,** 188–207.

Cheon, Y., Ha, S., Lee, S. & Son, M., 2020. Tectonic evolution of the Cretaceous Gyeongsang Back-arc Basin, SE Korea: transition from sinistral transtension to strike-slip kinematics, *Gondwana Res.,* **83,** 16–35.

Cheon, Y., Son, M., Song, C.W., Kim, J.S. & Sohn, Y.K., 2012. Geometry and kinematics of the Ocheon Fault System along the boundary between the miocene Pohang and Janggi basins, SE Korea, and its tectonic implications, *Geosci. J.,* **16**(3), 253–273.

Cho, H., Son, M., Cheon, Y., Sohn, Y.K., Kim, J.-S. & Kang, H.-C., 2016. Evolution of the Late Cretaceous Dadaepo Basin, SE Korea, in response to oblique subduction of the proto-Pacific (Izanagi/Kula) or Pacific plate, *Gondwana Res.,* **39,** 145–164.

Choi, H.O., Choi, S.H. & Kim, S.S., 2021. Zircon U-Pb geochronology and Sr–Nd–Pb–Hf isotope geochemistry for permian–Early triassic arc-related magmatism in Pohang, Jangsari, and Yeongdeok, southeastern Korean Peninsula, *Lithos,* **382–383,** 105930.

Choi, H.O., Choi, S.H., Lee, D.C. & Kang, H.C., 2013. Geochemical evolution of basaltic volcanism within the tertiary basins of southeastern Korea and the opening of the East Sea (Sea of Japan), *J. Volc. Geotherm. Res.,* **249,** 109–122.

Choi, J.H., Yang, S.J., Han, S.R. & Kim, Y.S., 2015. Fault zone evolution during cenozoic tectonic inversion in SE Korea, *J. Asian Earth Sci.,* **98,** 167–177.

Choi, S., Kim, S.W., Yoon, J.S. & Choi, E.K., 2023. Tectonic evolution of the Yangsan Fault, SE-Korea, by gravity field interpretation, *Geophys. J. Int.,* **235**(1), 287–295.

Chough, S., Kwon, S.-T., Ree, J.-H. & Choi, D.K., 2000. Tectonic and sedimentary evolution of the Korean Peninsula: a review and new view, *Earth-Sci. Rev.,* **52**(1–3), 175–235.

Chough, S.K. & Sohn, Y.K. 2010, Tectonic and sedimentary evolution of a cretaceous continental arc–backarc system in the Korean peninsula: new view, *Earth Sci. Rev.,* **101**(3–4), 225–249.

Christensen, N.I., 1996. Poisson's ratio and crustal seismology, *J. geophys. Res.,* **101**(2), 3139–3156.

Christensen, N.I. & Mooney, W.D., 1995. Seismic velocity structure and composition of the continental crust: a global view, *J. geophys. Res.,* **100**(B6), 9761–9788.

Chung, T.W. & Kim, W.H., 2000. Fault plane solutions for the June 26, 1997 Kyong-ju earthquake, *J. Korean Geophys. Soc.,* **3**(4), 245–250.

Ding, P., Wang, D., Di, G. & Li, X., 2019. Investigation of the effects of fracture orientation and saturation on the vp/vs ratio and their implications, *Rock Mech. Rock Eng.,* **52**(9), 3293–3304.

Faulkner, D.R., Jackson, C.A.L., Lunn, R.J., Schlische, R.W., Shipton, Z.K., Wibberley, C.A.J. & Withjack, M.O., 2010. A review of recent developments concerning the structure, mechanics and fluid flow properties of fault zones, *J. Struct. Geol.,* **32**(11), 1557–1575.

Finzi, Y., Hearn, E.H., Lyakhovsky, V. & Gross, L., 2011. Fault-zone healing effectiveness and the structural evolution of strike-slip fault systems, *Geophys. J. Int.,* **186**(3), 963–970.

Frederiksen, A.W. & Bostock, M.G., 2000. Modelling teleseismic waves in dipping anisotropic structures, *Geophys. J. Int.,* **141**(2), 401–412.

Goldstein, P. & Snoke, A., 2005. SAC availability for the IRIS community, *IRIS Newsl,* **7**(1), 1–2.

Han, J., Seo, K.J., Kim, S., Sheen, D.H., Lee, D. & Byun, A.H., 2024. Research catalog of inland seismicity in the southern Korean Peninsula from 2012 to 2021 using deep learning techniques, *Seismol. Res. Lett.,* **95**(2A), 952–968.

Heo, D. *et al.* 2024. New insights on seismic activity in the southeastern Korean Peninsula from the Gyeongju Hi-density Broadband Seismic Network (GHBSN), *Geosci. J.,* **28**(3), 319–333.

Hunter, J.D., 2007. Matplotlib: a 2D graphics environment, *Comput. Sci. Eng.,* **9**(3), 90–95.

Hwang, B.H., McWilliams, M., Son, M. & Yang, K., 2007. Tectonic implication of A-type granites across the Yangsan fault, Gigye and

Gyeongju areas, southeast Korean Peninsula, *Int. Geol. Rev.,* **49**(12), 1094–1102.

Hwang, B.H., Son, M., Yang, K., Yoon, J. & Ernst, W.G., 2008. Tectonic evolution of the Gyeongsang Basin, southeastern Korea from 140 Ma to the present, based on a strike-slip and block rotation tectonic model, *Int. Geol. Rev.,* **50**(4), 343–363.

Jo, E. & Hong, T.K., 2013. Vp/vs ratios in the upper crust of the southern Korean Peninsula and their correlations with seismic and geophysical properties, *J. Asian Earth Sci.,* **66,** 204–214.

Jolivet, L., Fournier, M., Huchon, P., Rozhdestvenskiy, V.S., Sergeyev, K.F. & Oscorbin, L.S., 1992. Cenozoic intracontinental dextral motion in the Okhotsk-Japan Sea region, *Tectonics,* **11**(5), 968–977.

Jolivet, L., Tamaki, K. & Fournier, M., 1994. Japan Sea, opening history and mechanism: a synthesis, *J. geophys. Res.,* **99**(B11), 22 237–22 259.

Katz, O. & Reches, Z., 2004. Microfracturing, damage, and failure of brittle granites, *J. geophys. Res.,* **109**(B1), B01206.

Kee, W.-S. *et al.* 2019. *1:1,000,000-scale Geologic Map of Korea,* Korea Institute of Geoscience and Mineral Resources (KIGAM).

Kennett, B.L.N. & Engdahl, E.R., 1991. Traveltimes for global earthquake location and phase identification, *Geophys. J. Int.,* **105**(2), 429–465.

Kim, C.M., Cheon, Y., Lee, T.H., Choi, J.H., Ha, S. & Jeong, J.O., 2022. Long-term weakening processes and short-term seismic slip behavior of an intraplate mature fault zone: a case study of the Yangsan Fault, SE Korea, *J. geophys. Res.,* **127**(4), e2021JB023154.

Kim, H. *et al.* 2024. Latent magmatism beneath the Korean Peninsula caused by asthenosphere upwelling, *Commun. Earth Environ.,* **5**(1), 15.

Kim, H.C. & Lee, Y., 2007. Heat flow in the Republic of Korea, *J. geophys. Res.,* **112**(B5), B05411.

Kim, I.-S., Son, M., Jung, H.-J., Lee, J.-D., Kim, J.-J. & Paik, I.S., 1998. Geological characteristics of Kyongju-Ulsan area: palaeomagnetism and magnetic susceptibility of the granitic rocks in the Ulsan Fault area, *Econ. environ. Geol.,* **31**(1), 31–43 (in Korean with English abstract).

Kim, J.-C. *et al.* 2002. *1:250,000-scale Digital Geological Map of Korea,* Korea Institute of Geoscience and Mineral Resources (KIGAM).

Kim, K., Oh, S., Kwon, H.S., Lee, S.K. & Chung, H., 2023. Two-dimensional interpretation of audio-magnetotelluric data around the epicentre distribution of the 2016 Gyeongju earthquake (ML 5.8), *Korea, Geosci. J.,* **27**(5), 563–580.

Kim, K.-H. *et al.* 2018. Deep fault plane revealed by high-precision locations of early aftershocks following the 12 September 2016 ML 5.8 Gyeongju, Korea, earthquake, *Bull. seism. Soc. Am.,* **108**(1), 517–523.

Kim, M., Lim, H. & Kim, Y., 2025. *Teleseismic waveform data and P receiver functions from the Gyeongju Hi-density Broadband Seismic Network (GHBSN),* [Dataset], Zenodo.

Kim, N., Park, S.I., Cho, C.S., Cheon, Y. & Peace, A.L., 2023. Neotectonic transpressional intraplate deformation in eastern Eurasia: insights from active fault systems in the southeastern Korean Peninsula, *Geosci. Front.,* **14**(4), 101559.

Kim, S., Tkalčić, H., Rhie, J. & Chen, Y., 2016. Intraplate volcanism controlled by back-arc and continental structures in NE Asia inferred from transdimensional Bayesian ambient noise tomography, *Geophys. Res. Lett.,* **43**(16), 8390–8398.

Kim, Y., He, X., Ni, S., Lim, H. & Park, S.-C., 2017. Earthquake source mechanism and rupture directivity of the 12 September 2016 M_w 5.5 Gyeongju, South Korea, earthquake, *Bull. seism. Soc. Am.,* **107**(5), 2525–2531.

Kim, Y., Rhie, J., Kang, T.-S., Kim, K.-H., Kim, M. & Lee, S.J., 2016. The 12 September 2016 Gyeongju earthquakes: 1. Observation and remaining questions, *Geosci. J.,* **20**(6), 747–752.

Lallemand, S. & Jolivet, L., 1986. Japan Sea: a pull-apart basin?, *Earth planet. Sci. Lett.,* **76**(3–4), 375–389.

Langston, C.A., 1979. Structure under Mount Rainier, Washington, inferred from teleseismic body waves, *J. geophys. Res.,* **84**(B9), 4749–4762.

Lee, H., Kim, H., Kagoshima, T., Park, J.-O., Takahata, N. & Sano, Y., 2019. Mantle degassing along strike-slip faults in the southeastern Korean Peninsula, *Sci. Rep.,* **9**(1), 16011.

Lee, S. *et al.* 2023. Crustal and uppermost mantle structures imaged by teleseismic *P*-wave traveltime tomography beneath the southeastern Korean Peninsula: implications for a hydrothermal system controlled by the thermally modified lithosphere, *Geophys. J. Int.,* **235**(2), 1639–1657.

Lee, Y., Park, S., Kim, J., Kim, H.C. & Koo, M.-H., 2010. Geothermal resource assessment in Korea, *Renew. Sustainable Energy Rev.,* **14**(8), 2392–2400.

Lee, Y.I., Lee, J.I. & Choi, Y.S., 2023. Provenance analysis of the Cretaceous Gyeongsang Basin, SE Korea: a synthesis and tectonic implications for active continental margin in East Asia, *Earth-Sci. Rev.,* **238,** 104334.

Lee, Y.S., Ishikawa, N. & Kim, W.K., 1999. Palaeomagnetism of tertiary rocks on the Korean Peninsula: tectonic implications for the opening of the East Sea (Sea of Japan), *Tectonophysics,* **304**(1–2), 131–149.

Lewis, M.A. & Ben-Zion, Y. 2010, Diversity of fault zone damage and trapping structures in the Parkfield section of the San Andreas Fault from comprehensive analysis of near fault seismograms, *Geophys. J. Int.,* **183**(3), 1579–1595.

Li, H., Ye, Z., Gao, R. & Huang, X., 2022. A distinct contrast in the lithospheric structure and limited crustal flow across the northeastern Tibetan Plateau: evidence from *Vs* and *Vp*/*Vs* imaging, *Tectonophysics,* **836,** 229413.

Li, J., Song, X., Wang, P. & Zhu, L., 2019. A generalized H-κ method with harmonic corrections on *Ps* and its crustal multiples in receiver functions, *J. geophys. Res.,* **124**(4), 3782–3801.

Ligorría, J.P. & Ammon, C.J., 1999. Iterative deconvolution and receiver-function estimation, *Bull. seism. Soc. Am.,* **89**(5), 1395–1400.

Liu, H. & Niu, F., 2012. Estimating crustal seismic anisotropy with a joint analysis of radial and transverse receiver function data, *Geophys. J. Int.,* **188**(1), 144–164.

Liu, K., Zhang, J., Xiao, W., Wilde, S.A. & Alexandrov, I., 2020. A review of magmatism and deformation history along the NE Asian margin from ca. 95 to 30 ma: transition from the Izanagi to Pacific plate subduction in the early Cenozoic, *Earth-Sci. Rev.,* **209,** 103317.

Liu, S., Gurnis, M., Ma, P. & Zhang, B., 2017. Reconstruction of northeast Asian deformation integrated with western Pacific plate subduction since 200 ma, *Earth-Sci. Rev.,* **175,** 114–142.

Liu, X. & Zhao, D., 2016. Backarc spreading and mantle wedge flow beneath the Japan Sea: insight from Rayleigh-wave anisotropic tomography, *Geophys. J. Int.,* **207**(1), 357–373.

Maeda, T., Takemura, S. & Furumura, T., 2017. OpenSWPC: an open-source integrated parallel simulation code for modelling seismic wave propagation in 3-D heterogeneous viscoelastic media, *Earth Planets Space,* **69**(1), 102.

Marchesini, B., Pozzi, G., Collettini, C., Carminati, E. & Tesei, T., 2025. Caprock genesis in hydrothermal systems via alteration-controlled fault weakening and impermeabilization, *J. geophys. Res.,* **130**(2), e2024JB030565.

Otofuji, Y.-I. & Matsuda, T., 1983. Palaeomagnetic evidence for the clockwise rotation of Southwest Japan, *Earth planet. Sci. Lett.,* **62**(3), 349–359.

Otofuji, Y.-I. & Matsuda, T., 1987. Amount of clockwise rotation of Southwest Japan: fan-shape opening of the southwestern part of the Japan Sea, *Earth planet Sci. Lett.,* **85**(1–3), 289–301.

Otofuji, Y.-I., Matsuda, T. & Nohda, S., 1985. Opening mode of the Japan Sea inferred from the palaeomagnetism of the Japan Arc, *Nature,* **317**(6038), 603–604.

Park, S. & Hong, T.K., 2024. Continent-side uplifted mantle and geological imprints along a palaeo rift in the western East Sea (Sea of Japan), *J. geophys. Res.,* **129**(9), e2024JB029049.

Park, Y., Ree, J.-H. & Yoo, S.-H., 2006. Fault slip analysis of quaternary faults in southeastern Korea, *Gondwana Res.,* **9**(1–2), 118–125.

Ree, J.-H., Lee, Y.-J., Rhodes, E.J., Park, Y., Kwon, S.-T., Chwae, U., Jeon, J.-S. & Lee, B., 2003. Quaternary reactivation of tertiary faults in the southeastern Korean Peninsula: age constraint by optically stimulated luminescence dating, *Island Arc,* **12**(1), 1–12.

Rondenay, S., 2009. Upper mantle imaging with array recordings of converted and scattered teleseismic waves, *Surv. Geophys.,* **30**(4–5), 377–405.

Sammis, C.G. & Ben-Zion, Y., 2008. Mechanics of grain-size reduction in fault zones, *J. geophys. Res.,* **113**(B2), B02306.

Schulte-Pelkum, V. & Ben-Zion, Y., 2012. Apparent vertical Moho offsets under continental strike-slip faults from lithology contrasts in the seismogenic crust, *Bull. seism. Soc. Am.,* **102**(6), 2757–2763.

Schulte-Pelkum, V. & Mahan, K.H., 2014. A method for mapping crustal deformation and anisotropy with receiver functions and first results from USArray, *Earth planet. Sci. Lett.,* **402,** 221–233.

Seo, M.-S., Son, Y.O., Kim, Y., Kang, T.-S., Rhie, J., Kim, K.-H. & Ree, J.-H., 2022. Measurement of seismometer misorientation based on P-wave polarization: application to dense temporary broadband seismic array in the epicentral region of the 2016 Gyeongju earthquake, South Korea, *Geosci. J.,* **26**(3), 385–397.

Seton, M. *et al.* 2012. Global continental and ocean basin reconstructions since 200 ma, *Earth-Sci. Rev.,* **113**(3–4), 212–270.

Shi, D., Shen, Y., Zhao, W. & Li, A., 2009. Seismic evidence for a Moho offset and south-directed thrust at the easternmost Qaidam-Kunlun boundary in the northeast Tibetan Plateau, *Earth planet. Sci. Lett.,* **288**(1–2), 329–334.

Shim, S.-H., Park, B.-J., Kim, T.-H., Jang, Y.-D., Kim, J.-H. & Kim, J.-J., 2011. Petrology of the tertiary basaltic rocks in the Yeonil and Eoil basins, southeastern Korea, *J. Petrol. Soc. Korea,* **20**(1), 1–21.

Soh, I., Chang, C., Lee, J., Hong, T.K. & Park, E.S., 2018. Tectonic stress orientations and magnitudes, and friction of faults, deduced from earthquake focal mechanism inversions over the Korean Peninsula, *Geophys. J. Int.,* **213**(2), 1360–1373.

Sohn, Y.K., 2000. Depositional processes of submarine debris flows in the miocene fan deltas, Pohang Basin, SE Korea, with special reference to flow transformation, *J. Sediment. Res.,* **70**(3), 491–503.

Son, M., Song, C.W., Kim, M.C., Cheon, Y., Cho, H. & Sohn, Y.K., 2015. Miocene tectonic evolution of the basins and fault systems, SE Korea: dextral simple shear during the East Sea (Sea of Japan) opening, *J. geol. Soc. Lond.,* **172**(5), 664–680.

Tatsumi, Y., Otofuji, Y.-I., Matsuda, T. & Nohda, S., 1989. Opening of the Sea of Japan back-arc basin by asthenospheric injection, *Tectonophysics,* **166**(4), 317–329.

Tian, D. *et al.* 2024. *PyGMT: a Python interface for the Generic Mapping Tools (version 0.14.0)* [Software] Zenodo.

Van Horne, A., Sato, H. & Ishiyama, T., 2017. Evolution of the Sea of Japan back-arc and some unsolved issues, *Tectonophysics,* **710–711,** 6–20.

Wessel, P., Luis, J.F., Uieda, L., Scharroo, R., Wobbe, F., Smith, W.H.F. & Tian, D., 2019. The Generic Mapping Tools version 6, *Geochem. Geophys. Geosyst.,* **20**(11), 5556–5564.

Withjack, M.O. & Jamison, W.R. 1986. Deformation produced by oblique rifting, *Tectonophysics,* **126,** 99–124.

Woo, J.U., Rhie, J., Kim, S., Kang, T.-S., Kim, K.-H. & Kim, Y., 2019. The 2016 Gyeongju earthquake sequence revisited: aftershock interactions within a complex fault system, *Geophys. J. Int.,* **217**(1), 58–74.

Xu, M. & He, J., 2022. Seispy: python module for batch calculation and postprocessing of receiver functions, *Seismol. Res. Lett.,* **94**(2A), 935–943.

Yamamoto, T. & Hoang, N., 2009. Synchronous Japan Sea opening and Miocene fore-arc volcanism in the Abukuma Mountains, NE Japan: an advancing hot asthenosphere flow versus Pacific slab melting, *Lithos,* **112**(3–4), 575–590.

Yamaoka, K. & Wallis, S.R., 2023. Clockwise rotation of SW Japan and timing of Izanagi–Pacific ridge subduction revealed by arc migration, *Prog. Earth Planet. Sci.,* **10**(1), 46.

Yan, Z. & Clayton, R.W., 2007. A notch structure on the Moho beneath the Eastern San Gabriel Mountains, *Earth planet. Sci. Lett.,* **260**(3–4), 570–581.

Yang, G., Zhao, L.F., Xie, X.B., He, X., Yan, L. & Yao, Z.X., 2022. "Double door" opening of the Japan Sea inferred by Pn attenuation tomography, *Geophys. Res. Lett.,* **49**(16), e2022GL099886.

Yi, K., Cheong, C., Kim, J., Kim, N., Jeong, Y.J. & Cho, M., 2012. Late palaeozoic to early mesozoic arc-related magmatism in southeastern Korea: SHRIMP zircon geochronology and geochemistry, *Lithos,* **153,** 129–141.

Zertani, S., Thielmann, M. & Menegon, L., 2025. Lower-crustal earthquakes: strain rate controls the magnitude and rate of stress amplification in rigid blocks, *Geophys. Res. Lett.,* **52**(7), e2024GL114350.

Zheng, T., Ding, Z., Ning, J., Liu, K.H., Gao, S.S., Chang, L., Kong, F. & Fan, X., 2019. Crustal azimuthal anisotropy beneath the central North China Craton revealed by receiver functions, *Geochem. Geophys. Geosyst.,* **20**(5), 2235–2251.

Zhu, L. & Kanamori, H., 2000. Moho depth variation in southern California from teleseismic receiver functions, *J. geophys. Res.,* **105**(B2), 2969–2980.